GeoMicro3D

A novel numerical model for simulating the reaction process and microstructure formation of alkali-activated slag

Zuo, Yibing; Ye, Guang

DOI
10.1016/j.cemconres.2020.106328

Publication date
2021

Document Version
Accepted author manuscript

Published in
Cement and Concrete Research

Citation (APA)
Zuo, Y., & Ye, G. (2021). GeoMicro3D: A novel numerical model for simulating the reaction process and microstructure formation of alkali-activated slag. *Cement and Concrete Research*, *141*, 1-21. Article 106328. https://doi.org/10.1016/j.cemconres.2020.106328

Cement and Concrete Research, 141 (2021) 106328

GeoMicro3D: A novel numerical model for simulating the reaction process and microstructure formation of alkali-activated slag

Yibing Zuo[a,b,*] , Guang Ye[b]

[a]School of Civil and Hydraulic Engineering, Huazhong University of Science and Technology, Wuhan 430074, China

[b]Faculty of Civil Engineering and Geosciences, Delft University of Technology, Stevinweg 1, 2628 CN Delft, The Netherlands

Abstract: For the first time, this study developed a novel model, named GeoMicro3D, to simulate the reaction process and microstructure formation of alkali-**activated** slag. The GeoMicro3D model consists of four modules that are designed to simulate, respectively: (i) the initial spatial distribution of real-shape slag particles in alkaline activator, (ii) the dissolution of slag and diffusion of ions via the transition state theory **and** lattice Boltzmann method, respectively, (iii) the spatial distribution of reaction products using a nucleation probability theory, and (iv) the chemical reactions with thermodynamic modelling. Afterwards the GeoMicro3D model was implemented and verified. The simulation results were discussed and compared with the relevant experimental data and thermodynamic calculation results using GEMS. A good agreement was found in the comparisons, showing the strong simulation capability of GeoMicro3D.

Keywords: Numerical simulation; Alkali-activated slag; Reaction process; Microstructure formation; GeoMicro3D

---

* Corresponding author: zuoyibing@hust.edu.cn

1. Introduction

The alkali activation of vitreous ground granulated blast furnace slag (GGBFS) produces a kind of clinker-free cement, which is supposed to efficiently improve the sustainability of concrete production [1-4]. Compared with ordinary Portland cement (OPC), alkali-activated slag (AAS) cement has lower equivalent emissions of CO_2 [5-7] and exhibits similar or even better mechanical properties and durability performance [8, 9]. Most of these excellent properties are largely relied on the reaction process and microstructure formation of AAS.

With the rapid development of computer technology, numerical models have been well developed and widely used in the studies of OPC based materials, providing an important numerical study route besides the experimental study route [10, 11]. With the numerical models it is possible to simulate the hydration process and microstructure development, in particular of the pore structure in hardening OPC based materials. Table 1 lists four main numerical models and their characteristics for studying OPC based materials [12]. The reaction process and microstructure evolution of OPC based materials can be simulated through either of the three-dimensional cement hydration and microstructure development model (CEMHYD3D) [13], Navi's model [14] and three-dimensional hydration, morphology and structure formation model (HYMOSTRUC) [12, 15]. Furthermore, the durability of concrete model (DuCOM) and HYMOSTRUC can be used to investigate and predict not only the transport properties of water and ions in OPC concrete but also the corrosion and degradation of OPC concrete in the erosion environment [12, 16, 17].

Table 1 Comparison of the main features between four numerical models (after [12])

	CEMHYD3D	Navi's model	DuCOM	HYMOSTRUC
Particle size distribution	1~40 μm	6~60 μm	mono-size particles	no limitation
Particle shape	real-shape	sphere	sphere	sphere
Composition of cement	C_3S,C_2S,C_3A, C_4AF,gypsum	C_3S	C_3S	C_3S, C_2S
Type of cement	OPC, blended cement	×	OPC, medium heat cement, high belite cement	OPC, blended cement
Mixture proportion	√	×	√	√
Kinetics	×	√	√	√
Curing condition	temperature, moisture	×	temperature	temperature
Mineral admixture	filler	filler (mono-size)	filler	filler
Dimensions	3D	3D	3D	3D
Pore scale	capillary pore	capillary pore	capillary pore, gel pore	capillary pore
Reference	[13]	[14, 22]	[16]	[15]

Note: C_3S, C_2S, C_3A, C_4AF and OPC represent tricalcium silicate, dicalcium silicate, tricalcium aluminate, calcium ferroaluminate and ordinary Portland cement, respectively. "√"and "×" mean that the model considers and does not consider, respectively.

It is noted that the numerical models that are designed for OPC based materials, however, are not capable of simulating the reaction process and microstructure formation of AAS. In the literature the numerical studies of AAS mainly concentrate on the following two aspects:

- *Modelling the chemistry and structure of the C-(N-)A-S-H gels.* The alkali calcium-aluminosilicate hydrate, i.e. the C-(N-)A-S-H gel, is the primary reaction product in AAS [18]. Puertas et al. defined a tobermorite structure based model for describing the C-(N-)A-S-H gels and found that the structure of the C-(N-)A-S-H gels largely depended on the nature of the alkaline activator [19]. In another study, a generalized model named the cross-linked substituted tobermorite model (CSTM) was derived [20]. In this model a blend of cross-linked and non-cross-linked tobermorite-based structures were employed to simulate the C-(N-)A-S-H gels. Compared with the models that were based on the non-cross-linked tobermorite-based structure, the CSTM model was found to be more capable of simulating the composition and structure of the C-(N-)A-S-H gels. By coupling the numerical simulation and experimental study, the Al in cross-linking of the C-(N-)A-S-H gel was investigated in [21]. The numerical simulation was carried out by using the CSTM model and in the experimental study the ^{29}Si and ^{27}Al NMR spectroscopy was used. It was found that a longer reaction time resulted in a reduction of the Al/Si ratio in the C-(N-)A-S-H gels.

- *Thermodynamic modelling of the chemical reactions:* Myers et al. derived a calcium-alkali aluminosilicate hydrate ideal solid solution model, named CNASH_ss, and simulated the chemical reactions in AAS [23] (more details on the CNASH_ss model can be referred to Section 2.4). The simulation results showed that the calculated C-(N-)A-S-H gel densities and molar volumes agreed with their corresponding experimental values reported in the literature [24]. With the CNASH_ss model, the solid phase assemblage of AAS was simulated and a good consistency was found between the simulation results and the experimental data [25]. Based on the thermodynamic modelling results, Myers et al. determined the phase diagrams of AAS [26]. In another study, the CNASH_ss model was employed to simulate the solid phase composition and chemical shrinkage of AAS [27].

So far, however, there is a dearth of information on the numerical models that are capable of simulating the reaction process and microstructure formation of AAS. Nowadays it is still a big subject and problem for researchers to have a numerical model with which it is possible to numerically investigate the microstructure development of AAS. Due to the lack of a numerical model to obtain the microstructure, the researchers find it very difficult to numerically investigate many microstructure-related-physical-properties of AAS, such as tensile strength, permeability and diffusivity of chloride.

In this background, a novel numerical model, i.e. GeoMicro3D abbreviated from Geopolymer Microstructure 3 Dimensions, was developed for the first time in this study to simulate the reaction process and microstructure formation of AAS. The GeoMicro3D model was developed by strictly following the simulations of the initial spatial distribution of real-shape slag particles in alkaline activator, dissolution of slag, diffusion of ions, chemical reactions of ions and nucleation and growth of reaction products in AAS. After build-up of the GeoMicro3D model, it was implemented and then verified by the relevant experimental data and thermodynamic calculation results using GEMS. The GeoMicro3D model proposed in this study may serve as a numerical simulation tool, with which it is possible for researchers to numerically study and forecast many microstructure-related-physical-properties of AAS.

2. Methodology

The GeoMicro3D model consists of four modules as displayed in Fig. 1. The first module (①) generates the initial spatial distribution of real-shape slag particles in alkaline activator prior to the onset of reactions. The second module (②) simulates the dissolution of slag. The third module (③) simulates the spatial distribution of reaction products, in which a novel strategy is proposed to improve the computation efficiency. In the last module (④) the chemical reactions are described and the amounts of reaction products are determined via the thermodynamic modelling. The modules ②, ③ and ④ make up a loop in which the lattice Boltzmann method (LBM) is applied to describe the diffusion of ions.

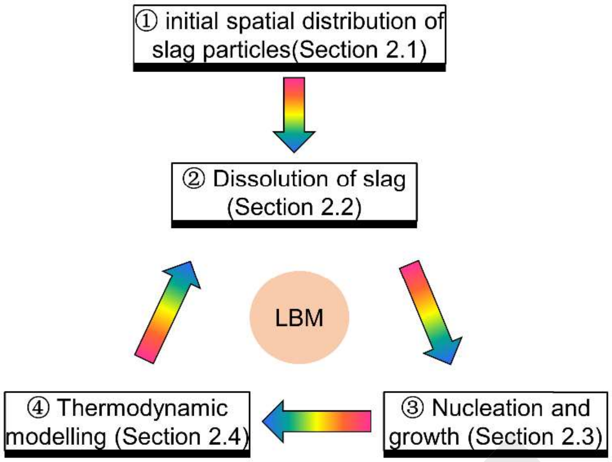

Fig. 1. Modules of the GeoMicro3D model. LBM represents lattice Boltzmann method.

2.1. Simulation of the initial spatial distribution of slag particles in alkaline activator

The initial spatial distribution of slag particles in alkaline activator is the starting point for performing numerical simulations of the reaction process and microstructure formation of AAS. Here the initial spatial distribution of slag particles in alkaline activator solution is defined as the state of slag particles in alkaline activator before the onset of reactions. In this study, a geometrical model, named Anm material model [28], was employed to simulate the initial spatial distribution of slag particles in alkaline activator using real-shape particles of slag.

In the Anm material model, particle shapes are described with spherical harmonic expansion coefficients a_{nm}, as expressed with Eq. (1) in a 3D spherical polar coordinate system.

$$r(\theta, \varphi) = \sum_{n=0}^{\infty} \sum_{m=-n}^{n} a_{nm} Y_{nm}(\theta, \varphi) \tag{1}$$

$$Y_{nm}(\theta, \varphi) = \sqrt{\frac{(2n+1)(n-m)!}{4\pi(n+m)!}} P_{nm}(\cos\theta) e^{im\varphi} \tag{2}$$

where:

- $r(\theta, \varphi)$ – the distance from the particle center of mass to the surface point

- $Y_{nm}(\theta, \varphi)$ – the spherical harmonic function

- θ – the polar angle

- φ – the azimuthal angle

- n, m – the indices ($-n \leq m \leq n$)

- $P_{nm}(cos\ \theta)$ – the associated Legendre polynomial [29]

- i – the square root of -1

The spherical harmonic expansion coefficients, i.e. a_{nm}, can be determined analytically from digital micro X-ray computed tomography images of slag particles [30]. Once a_{nm} is determined, then the particle shape can be described with Eqs. (1) and (2). As an example, Fig. 2 shows a real-shape particle of slag that is described by a_{nm}. The spherical harmonic expansion coefficients of different slag particles make up the particle shape database for slag.

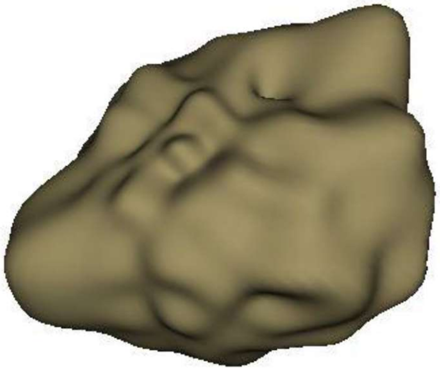

Fig. 2. A real-shape particle of slag described by the spherical harmonic coefficients. The particle width is 15.56 μm. (In this study, the particle width was used as the measure of particle size, see details in the text)

Once the spherical harmonic coefficients are known, many geometric properties can be calculated, such as the particle volume, surface area, length, width, and thickness [31]. Length is the longest surface-surface distance in the particle; width is the longest surface-surface distance in the particle such that width is perpendicular to length; and thickness is the longest surface-surface distance in the particle such that thickness is perpendicular to both length and width [31]. Since the particle width is thought to match best with the usual standard experimental sieve classification of particles [32, 33], it is preferentially used for computational sieve analysis [30]. In this study, the particle width was used as the measure of particle size.

In the simulation process, the particles are placed one after another into the cubic box. The cubic box, also noted as simulation box, represents the representative elementary volume (REV) for simulation and its size should not be smaller than 2.5 times of the largest slag particle [34]. The larger particles are processed before the smaller ones. So before the simulation, the particles are grouped into different particle size ranges. The particles within a larger particle size range are processed before the ones within a smaller particle size range. For placing the particles from a certain particle size range into the simulation box, the particle size is picked up stochastically within this particle size range and the particle shape is taken from the shape database of slag. In order to avoid overlapping with the particles that are already placed in the simulation box, stochastic trials are usually needed to look for the particle position and orientation. Full details on the modelling procedures and algorithms can be found in [28, 34, 35]. Fig. 3 shows one example of the simulated initial spatial distribution of real-shape slag particles in sodium hydroxide solution using the Anm material model. Ref. [36] provides more information about using the Anm material model to simulate the initial spatial distribution of real-shape slag particles in sodium hydroxide solution.

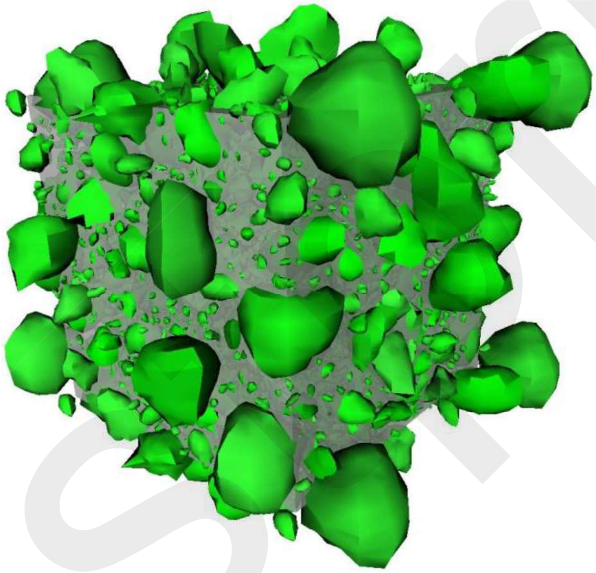

Fig. 3. Simulated initial spatial distribution of real-shape slag particles in sodium hydroxide solution using the Anm material model. The size of the simulation box was 125 μm × 125 μm × 125 μm. The liquid to binder ratio was 0.59. More information can be found in [36].

2.2. Simulation of the dissolution of slag

When slag is brought into contact with the alkaline activator solution, the dissolution of element constituents in slag starts and the transport of the released ions starts by diffusion. In this study, therefore, the simulation of the dissolution of slag can be divided into two main aspects: one is to simulate the dissolution of the element constituents in slag by using the transition state theory (see the following subsection 2.2.1), and the other is to simulate the diffusion of the released ions by using the lattice Boltzmann (LB) method (see the following subsection 2.2.2). Based on these two steps, the dissolved amount of element at each LB simulation step can be obtained (see the following subsection 2.2.3). The amount of the dissolved elements then serve as source terms and participate in the LB simulation in the next LB simulation step. As a demonstration example, Fig. 4 shows the simulated progressing dissolution of one real-shape slag particle in alkaline solution by the *dissolution module*.

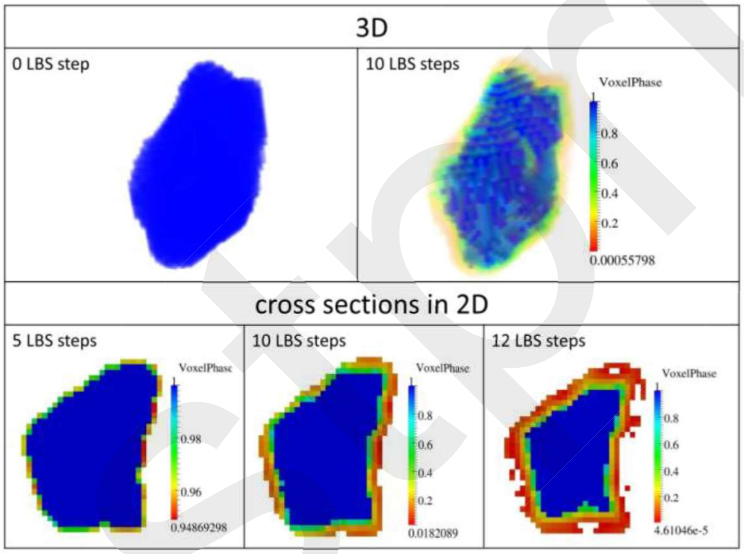

Fig. 4. Progressing dissolution of one real-shape slag particle in alkaline solution. LBS refers to lattice Boltzmann simulation.

2.2.1. Simulation of the dissolution of the element constituents in slag

In aluminosilicate materials including slag, Si and Al build up the framework while alkali and alkali-earth metals like Ca and Mg modify the framework [37, 38]. So the alkali and alkali-earth metals are also called modifying elements. The framework refers to the glass network in aluminosilicate materials. In the framework Si and Al are tetrahedrally coordinated. As schematically shown in Fig. 5, the dissolution of slag can be described via the following four consecutive steps [39-41].

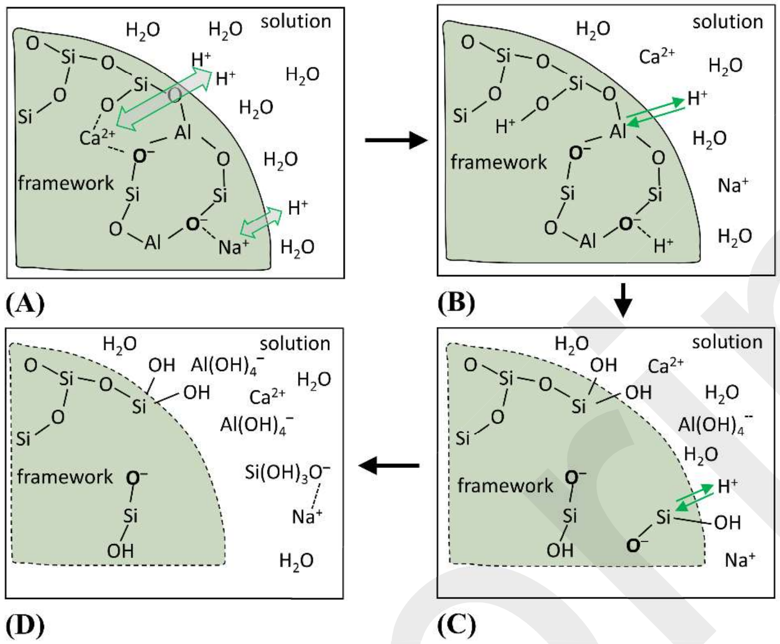

Fig. 5. Schematic illustration of the dissolution of slag (after [41]). For clarity, additional bonds between Si and O as well as between Al and O are not shown.

(i) First, the modifying elements are initially released through the metal/proton exchange reactions, as shown in Fig. 5(A).

(ii) Then, hydrolysis of the bonds between Al and O starts, as shown in Fig. 5(B).

(iii) Afterwards, the bonds between Si and O start to break, as shown in Fig. 5(C).

(iv) Finally, Al and Si are released, as a result of which the framework is gradually dissolved, as shown in Fig. 5(D).

Due to the smaller bonding energy of Al-O than Si-O, Al dissolves more easily than Si in the dissolution of slag [47]. The initially dissolved Al changes the adjoined Si coordination condition from fully coordinated to partially coordinated (Fig. 5(C)). Compared with the fully coordinated Si, the partially coordinated Si dissolves faster. So the dissolution of framework can be divided into the following two steps: initial dissolution of a small amount of Al (Fig. 5(B)) and then followed by the dissolution of Si that coordinates to the initially dissolved Al through O (Fig. 5(C)).

It is reported that the relative dissolution rate of each oxide within a multioxide phase equals to the dissolution rate of the single oxide [42, 43]. This is mostly due to the fact that the dissolution of glass is actually through the break of bonds between oxygen and other elements, such as Si-O, Al-O and Ca-O bonds, as shown in Fig. 5. That is to say, the simulation of the dissolution of the element constituents in slag can be carried out by simulating the dissolution of single element oxide. It should be noted that simulating the dissolution of glass in view of its individual oxide component is based on the assumption that the effect of mixing of multioxide on the Gibbs energy is negligible. How the mixing affects the Gibbs energy and how much the effect are in need of further research. The dissolution reactions of silica, aluminum and calcium oxide in alkaline solution can be described as follows:

$$SiO_2 + 2OH^- \rightarrow H_2O + {SiO_3}^{2-} \tag{3}$$

$$\mathrm{Al_2O_3 + 2OH^- \rightarrow H_2O + 2{AlO_2}^-} \tag{4}$$

$$CaO + H_2O \rightarrow 2OH^- + Ca^{2+} \tag{5}$$

According to the transition state theory, the dissolution rates of silica, aluminum and calcium oxide, i.e. r_{Si}, r_{Al} and r_{Ca}, can be obtained as expressed in the following equations. More details on the transition state theory and derivation of the following equations can be found in Appendix A.

$$r_{Si} = r_{+,Si}\left(1 - \left(\frac{IAP_{Si}}{K_{sp,Si}}\right)^{1/\sigma}\right) \quad (6)$$

$$r_{Al} = r_{+,Al}\left(1 - \left(\frac{IAP_{Al}}{K_{sp,Al}}\right)^{1/\sigma}\right) \quad (7)$$

$$r_{Ca} = r_{+,Ca}\left(1 - \left(\frac{IAP_{Ca}}{K_{sp,Ca}}\right)^{1/\sigma}\right) \quad (8)$$

where $r_{+,X}$, $K_{sp,X}$, and IAP_X are forward dissolution rate, solubility product and ion activity product of X, respectively. X can be silica, alumina or calcium oxide. IAP_X can be determined as follows according to Eqs. (3-5):

$$IAP_{Si} = \frac{a_{SiO_3{}^{2-}} * a_{H_2O}}{a_{OH^-} * a_{OH^-}} \quad (9)$$

$$IAP_{Al} = \frac{a_{AlO_2{}^-} * a_{AlO_2{}^-} * a_{H_2O}}{a_{OH^-} * a_{OH^-}} \quad (10)$$

$$IAP_{Ca} = \frac{a_{Ca^{2+}} * a_{OH^-} * a_{OH^-}}{a_{H_2O}} \quad (11)$$

where a_i represents the ion activity. i can be $SiO_3{}^{2-}$, $AlO_2{}^-$, Ca^{2+}, H_2O or OH^-.

According to the stoichiometric dissolution of Al and Si in aluminosilicate materials [44, 45], the log forward dissolution rates of Si and Al can be correlated as follows:

$$Log\ \ r_{+,Al} = Log\left(\frac{v_{Al}}{v_{Si}} r_{+,Si}\right) = Log\left(\frac{v_{Al}}{v_{Si}}\right) + Log\ \ r_{+,Si} \qquad (12)$$

where v_{Si} and v_{Al} are the molar fractions of Si and Al in slag, respectively.

In slag the contents of Mg, Na, K and S are small. Similar to Ca, these modifying elements also dissolve relatively fast in comparison with the tetrahedrally coordinated Si and Al in the framework. Therefore, the dissolution rates of Mg, Na, K and S can be determined as follows, by taking r_{Ca} as the reference.

$$r_{Mg} = f_{Mg} \cdot \frac{v_{Mg}}{v_{Ca}} \cdot r_{Ca} \qquad (13)$$

$$r_{Na} = f_{Na} \cdot \frac{v_{Na}}{v_{Ca}} \cdot r_{Ca} \qquad (14)$$

$$r_{K} = f_{K} \cdot \frac{v_{K}}{v_{Ca}} \cdot r_{Ca} \qquad (15)$$

$$r_{S} = f_{S} \cdot \frac{v_{S}}{v_{Ca}} \cdot r_{Ca} \qquad (16)$$

where r_{Mg}, r_{Na}, r_K and r_S are the dissolution rates of Mg, Na, K and S, respectively. f_{Mg}, f_{Na}, f_K and f_S are ratios of r_{Mg}, r_{Na}, r_K and r_S relative to r_{Ca}, respectively. v_{Ca}, v_{Mg}, v_{Na}, v_K and v_S are molar fractions of Ca, Mg, Na, K and S in slag, respectively.

2.2.2. Simulation of the diffusion of ions

As originated from the lattice gas automata, LB method is considered as a simplified version of molecular dynamics method, utilizing a discrete space, discrete time and discrete velocities [46]. It has been found that the LB method is a powerful method for solving fluid dynamics and ionic transport problems [46-48]. In this study, the LB method was employed to describe the diffusion of ions. The ions that are accounted for in the GeoMicro3D model are SiO_3^{2-}, AlO_2^-, Ca^{2+}, Mg^{2+}, K^+, Na^+, S^{2-} and OH^-. For modelling the mass transport in 3D, the D3Q19 model is commonly applied. D*d*Q*q* refers to a lattice structure with *q* lattice directions in *d* dimensions. The lattice structure defines the path for streaming of distribution function from current lattice cell to the neighboring lattice cell. When simulating the entirely diffusive mass transport, however, it is possible to decrease the velocity directions from 19 (D3Q19) to 7 (D3Q7) without affecting the simulation quality very much [49]. It is known that there is no convection in the reaction process of cement-based materials. So the transport of ions can be described as entirely diffusive mass transport [46]. For the purpose of decreasing the computation efforts and increasing the computation efficiency, the D3Q7 model was applied in the GeoMicro3D model to describe the diffusion of ions in AAS. The LB equation below describes the development of particle distribution function [47]:

$$f_i(x + e_i\delta_t, t + \delta_t) = f_i(x, t) - \frac{\delta_t}{\tau}[f_i(x, t) - f_i^{eq}(x, t)] + \omega_i\delta_t S \qquad (17)$$

where:

- f_i – the non-equilibrium particle distribution function

- f_i^{eq} – the equilibrium particle distribution function
- x – the location
- t – the time
- i – the velocity i (in this study $i = 0, 1, 2, 3, 4, 5, 6$)
- τ – the relaxation time
- δ_t – the time step
- e_i – the microscopic velocity
- w_i – the weighting factor
- S – the source term

Without convection, f_i^{eq} can be determined via the equation below, in which F is the ion concentration in the lattice cell:

$$f_i^{eq}(x,t) = \omega_i F(x,t) \tag{18}$$

$$F(x + e_i\delta_t, t + \delta_t) = \sum_{i=0}^{6} f_i\,(x + e_i\delta_t, t + \delta_t) \tag{19}$$

Fig. 6 shows a flow diagram of the LB simulation. After initialization, the LB simulation begins with the determination of f_i^{eq} using Eq. (18). Then the source term (S) is determined according to Eq. (21). With f_i^{eq} and S, the collision process is executed to obtain ($f_i(x+e_i\delta_t, t+\delta_t)$) by using Eq. (17). Then $f_i(x+e_i\delta_t, t+\delta_t)$ streams in each direction of velocity. Afterwards, periodic boundary conditions are applied to determine the $f_i(x+e_i\delta_t, t+\delta_t)$ of the lattice cells on the boundaries of the simulation box. Finally, ion concentrations are renewed according to Eq. (19). If the current time (T) exceeds the target reaction period (T_{target}) or the source terms are zero (S=0), then the data are quantified as output and the loop will stop; otherwise, the loop goes to the next LB simulation iteration.

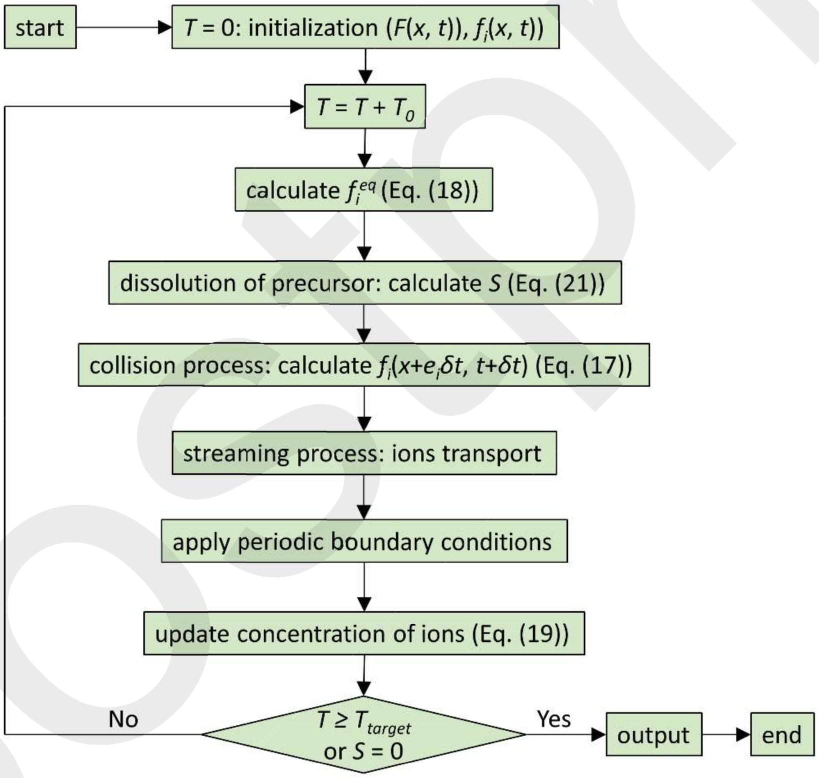

Fig. 6. Flow diagram of LB simulation of the dissolution of slag.

2.2.3. Dissolved amount of elements at each LB simulation step

In the digitization process, the voxels that are outside the slag particles are regarded as alkaline activator voxels and the rest voxels are taken as slag voxels. After digitization the simulation box becomes a box of voxels (or lattice cells). Therefore, the slag particles in the digitized simulation box actually consist of voxels. Due to the amorphous nature of slag, it is reasonable to assume an even distribution of element constituents in slag. That is to say, the element constituents in each slag voxel can be supposed identical to the chemical composition of slag. To simulate the dissolution of slag is actually to simulate the dissolution of element constituents in slag voxels.

For each slag voxel, there are six interfaces on which dissolution may take place. On each interface, the amount of elements that are released at one LB time step can be determined according to Eq. (20). The parameter $f_{dissolving\text{-}area}$ represents the area fraction of the interface that is being dissolved. In determining the dissolution rates using Eqs. (6-8) for the dissolving interface, the *IAP* is obtained based on the contacting neighbor voxel. With the amount of elements that are released on each interface, the total released amount of elements on six interfaces can be determined via Eq. (21). The dissolved amount of elements at one LB time step will participate in the collision step through the source term in Eq. (17) in the next LB simulation step.

$$\Delta n_{Y,i} = f_{dissolving-area} \cdot r_{Y,i} \cdot t_0 \cdot {l_0}^2 \qquad (20)$$

$$\Delta N_Y = \sum_{i=1}^{6} \Delta n_{Y,i} \qquad (21)$$

where:

- $\Delta n_{Y,i}$ – the released amount of element *Y* on interface *i*

- ΔN_Y – the released amount of element Y on six interfaces
- t_0 – one LB step time
- Y – an element that can be Si, Al, Ca, Mg, S or K
- $r_{Y,i}$ – the dissolution rate of element Y on the interface i
- l_0 – the side length of voxel

2.3. Simulation of the nucleation and growth of reaction products

With dissolution of slag, the concentrations of ions in the solution increase continuously. When the pore solution of AAS reaches saturation or oversaturation, reaction products are likely to precipitate. Whether the precipitation will occur or not depends on the nucleation condition in the pore solution. Nucleation is the statistical process of appearance of nanoscopically small clusters of molecules of a new phase in a supersaturated solution [50], which is the key step for the growth of reaction products. Eq. (22) is used to calculate the probability $P(t)$ that at least one critical nucleus exists in the solution [51]. Once at least one critical nucleus exists in the solution, the reaction product of this kind of nucleus begins to deposit and grow.

$$P(\Delta t) = 1 - \exp(-J \cdot V \cdot \Delta t) \qquad (22)$$

where V is the solution volume, Δt is the time interval and J is the nucleation rate that can be determined as follows [50, 51]:

$$J(S) = A \cdot S \cdot \exp(-\frac{B}{ln^2 S}) \quad (23)$$

where A and S are the kinetic parameter and supersaturation ratio, respectively, and B is the thermodynamic parameter that can be obtained for heterogeneous nucleation, as follows:

$$B = \frac{4}{27}\frac{c^3 \cdot v^2 \cdot \gamma_{ef}^3}{k_B^3 \cdot T^3} \quad (24)$$

Where:

- c – a shape factor ($(36\pi)^{1/3}$ for spheres and 6 for cubes)
- v – the molecular volume of the phase
- k_B – the Boltzmann constant
- T – the absolute temperature
- γ_{ef} – the effective interfacial energy, where $\gamma_{ef} = \psi\gamma$ with interfacial energy γ and activity factor $0 < \psi < 1$, and $\psi = 1$ for homogeneous nucleation

The γ can be determined with Eq. (25) below [50, 51]:

$$\gamma = \beta_N \cdot k_B \cdot T \cdot \frac{1}{v^{2/3}} \cdot \ln(\frac{1}{N_a \cdot v \cdot c^*}) \tag{25}$$

where β_N is a numerical factor ($\beta_N = 0.514$ for spherical nuclei), N_a is Avogadro's number and c^* (mol/L) is the molar solubility.

In a voxel without reaction products, it is possible for each reaction product to precipitate. In other words the nucleation probability should be calculated for each reaction product via Eq. (22) and the corresponding reaction should be simulated if the reaction product is predicted to precipitate. This, however, would result in a huge rise of the computation efforts and inevitably and dramatically reduce the computation efficiency. In fact the reaction products are actually finely mixed up with each other at the micro level according to experimental observation from the scanning electron microscopy (SEM) images [52-54]. Therefore it is not wise and necessary to simulate the precipitation and reaction of each reaction product separately at the micro level. For the purpose of limiting the computational load and respecting the experimental insights, a novel strategy was conceived and implemented in this study. The details of this novel strategy are described as follows.

The reaction products in AAS are classified into primary reaction products (C-(N-)A-S-H gel) and secondary reaction products (see details in Section 2.4). The deposit of reaction products is controlled to take place only when at least one of the eight CNASH_ss end-members and at least one of secondary reaction products are simulated to precipitate. For the voxels where reaction products will deposit, the *thermodynamic modelling module* is applied to simulate the reactions and calculate the amount of reaction products. The full procedure consists of four steps below and is displayed in Fig. 7.

a. Calculate the nucleation probabilities, P_X, P_Y and P_Z for primary reaction products and P_A, P_B and P_C for secondary reaction products, using Eq. (22).

b. Generate a random probability $0 \leq P_{random} \leq 1$.

c. Calculate the numbers (i.e. N_p and N_s) of primary reaction products and secondary reaction products that are predicted to nucleate, respectively.

d. If $N_p \geq 1$ and $N_s \geq 1$, then the *thermodynamic modelling module* (Section 2.4) is called.

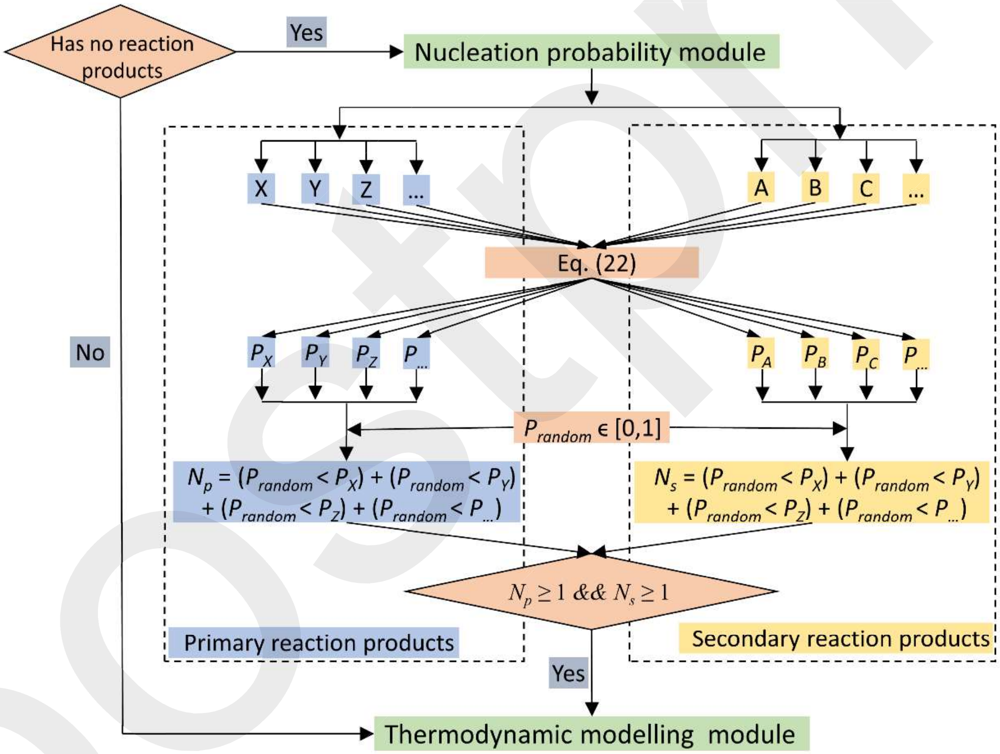

Fig. 7. Flowchart of nucleation probability module.

For a voxel that already has reaction products, the *thermodynamic modelling module* is applied directly without calling the *nucleation probability module*.

2.4. Thermodynamic modelling module

This module is applied to model the chemical reactions and determine the amounts of reaction products in AAS through thermodynamic modelling. The reaction products in AAS consist of primary reaction products, i.e. C-(N-)A-S-H gels [18], and secondary reaction products, such as hydrotalcite [55], tetracalcium aluminate hydrate (C_4AH_{13}) [55], katoite (C_3AH_6) [25], stratlingite (C_2ASH_8) [56] and portlandite (CH) [57] etc. Once the thermodynamic data of these reaction products are known, thermodynamic modelling of the reactions can be performed by using the thermodynamic program.

2.4.1. Thermodynamic data of the reaction products

(1) For the primary reaction products (C-(N-)A-S-H gels)

In this study the CNASH_ss model was used to describe the C-(N-)A-S-H gels. The CNASH_ss model contains eight CNASH_ss end-members. The dissociation reactions and thermodynamic data of these end-members are listed in Tables 2 and 3, respectively. More information on the derivation of the CNASH_ss model can be referred to [23].

Table 2 Dissociation reactions and solubility products (Log K_{sp}) for C-(N-)A-S-H and hydrotalcite-like phases at 25 °C and 1 bar.

Solids	Dissociation reactions	*Log K_{sp}*
CNASH_ss model [23]		
5CA	$(CaO)_{1.25}\cdot(Al_2O_3)_{0.125}\cdot(SiO_2)\cdot(H_2O)_{1.625} \leftrightarrow 1.25Ca^{2+} + SiO_3^{2-} + 0.25AlO_2^- + 0.25OH^- + 1.5H_2O$	-10.75
INFCA	$(CaO)\cdot(Al_2O_3)_{0.15625}\cdot(SiO_2)_{1.1875}\cdot(H_2O)_{1.65625} + 0.6875OH^- \leftrightarrow Ca^{2+} + 1.1875SiO_3^{2-} + 0.3125AlO_2^- + 2H_2O$	-8.90
5CNA	$(CaO)_{1.25}\cdot(Na_2O)_{0.25}\cdot(Al_2O_3)_{0.125}\cdot(SiO_2)\cdot(H_2O)_{1.25} \leftrightarrow 1.25Ca^{2+} + SiO_3^{2-} + 0.25AlO_2^- + 0.5Na^+ + 0.75OH^- + H_2O$	-10.40
INFCNA	$(CaO)\cdot(Na_2O)_{0.34375}\cdot(Al_2O_3)_{0.15625}\cdot(SiO_2)_{1.1875}\cdot(H_2O)_{1.3} \leftrightarrow Ca^{2+} + 1.1875SiO_3^{2-} + 0.3125AlO_2^- + 0.6875Na^+ + 1.3125H_2O$	-10.00
INFCN	$(CaO)\cdot(Na_2O)_{0.3125}\cdot(SiO_2)_{1.5}\cdot(H_2O)_{1.1875} + 0.375OH^- \leftrightarrow Ca^{2+} + 1.5SiO_3^{2-} + 0.625Na^+ + 1.375H_2O$	-10.70
T2C*	$(CaO)_{1.5}\cdot(SiO_2)\cdot(H_2O)_{2.5} \leftrightarrow 1.5Ca^{2+} + SiO_3^{2-} + OH^- + 2H_2O$	-11.60
T5C*	$(CaO)_{1.25}\cdot(SiO_2)_{1.25}\cdot(H_2O)_{2.5} \leftrightarrow 1.25Ca^{2+} + 1.25SiO_3^{2-} + 2.5H_2O$	-10.50
TobH*	$(CaO)\cdot(SiO_2)_{1.5}\cdot(H_2O)_{2.5} + OH^- \leftrightarrow Ca^{2+} + 1.5SiO_3^{2-} + 3H_2O$	-7.90
MA-OH-LDH_ss model [25]		
M_4AH_{10}	$(MgO)_4\cdot(Al_2O_3)\cdot(H_2O)_{10} \leftrightarrow 4Mg^{2+} + 2AlO_2^- + 6OH^- + 7H_2O$	-49.70
M_6AH_{12}	$(MgO)_6\cdot(Al_2O_3)\cdot(H_2O)_{12} \leftrightarrow 6Mg^{2+} + 2AlO_2^- + 10OH^- + 7H_2O$	-72.02
M_8AH_{14}	$(MgO)_8\cdot(Al_2O_3)\cdot(H_2O)_{14} \leftrightarrow 8Mg^{2+} + 2AlO_2^- + 14OH^- + 7H_2O$	-94.34

Table 3 Thermodynamic properties of the C(N)ASH_ss end-members at 25 °C and 1 bar.

Phase	V^0 (cm^3/mol)	$\Delta_f H^0$ (kJ/mol)	$\Delta_f G^0$ (kJ/mol)	S^0 (J/mol.K)	C_p^0 (J/mol.K)	Ref.
5CA	57.3	-2491	-2293	163	177	[23]
INFCA	59.3	-2551	-2343	154	181	[23]
5CNA	64.5	-2569	-2382	195	176	[23]
INFCNA	69.3	-2667	-2474	198	180	[23]
INFCN	71.1	-2642	-2452	186	184	[23]
T2C*	80.6	-2721	-2465	167	237	[23]
T5C*	79.3	-2780	-2517	160	234	[23]
TobH*	85.0	-2831	-2560	153	231	[23]

(2) For secondary reaction products

It is reported that the mackinawite (FeS) with unstable structure precipitates first and then it transforms to the mackinawite with stable structure and finally to pyrite or pyrrhotite [58]. Compared with other Fe-based phases, such as Fe-ettringite or $Fe(OH)_3$, mackinawite has higher stability in AAS [59]. In this study, the stable mackinawite is accounted for in the thermodynamic modelling of the reactions in AAS.

It is noted that the K_{sp} of hydrotalcite in [60, 61] are not in line with the values in [62]. This inconsistency has been found by Myers et al. [25]. In this situation, a thermodynamic model, i.e. MA-OH-LDH_ss, was derived for the hydrotalcite-like phases [25]. The MA-OH-LDH_ss model contains three solid phases (M_4AH_{10}, M_6AH_{12} and M_8AH_{14}) and their dissociation reactions are shown in Table 2.

Furthermore, CH, C_3AH_6, NAS_3H_2 and C_2ASH_8 are also accounted for in the thermodynamic modelling of the reactions in AAS. The thermodynamic data of all the considered secondary reaction products are presented in Table 4.

Table 4 Thermodynamic data of the considered secondary reaction products at 25 °C and 1 bar.

Phase	V^0 (cm^3/mol)	$\Delta_f H^0$ (kJ/mol)	$\Delta_f G^0$ (kJ/mol)	S^0 (J/mol.K)	C_p^0 (J/mol.K)	Ref.
Mackinawite, FeS	20.5	-92.0	-93.6	64.68	50.4	[63]
M_4AH_{10}	219	-7160	-6358	549	648	[25]
M_6AH_{12}	305	-9007	-8023	675	803	[25]
M_8AH_{14}	392	-10853	-9687	801	958	[25]
Portlandite, CH	33.1	-984.7	-897.0	83.4	87.5	[23]
Katoite, C_3AH_6	150	-5537	-5008	422	446	[64]
Natrolite, NAS_3H_2	169	-5728	-5325.7	360	359	[65]
Stratlingite, C_2ASH_8	216	-6360	-5705	546	603	[66]

2.4.2. Thermodynamic modelling program

Thermodynamic simulation was carried out using GEM-Selektor V3 (http://gems.web.psi.ch/) [67, 68]. GEM-Selektor V3 is a popularly employed thermodynamic program for doing thermodynamic calculations [23, 25, 26, 59, 61, 68-70]. The thermodynamic data used in this study consists of the basis thermodynamic database, i.e. the CEMDATA07 database reported in [70] and the thermodynamic data for reaction products reported in [23]. It is noted that the thermodynamic data for the primary reaction products, i.e. the C-(N-)A-S-H gel, and secondary reaction products in AAS are reproduced in Tables 3 and 4, respectively. The effectiveness of these thermodynamic data have been widely validated in the literature for CEMDATA07 [59, 61, 70] and for reaction products in AAS [23, 25-27, 57, 69].

In order to determine the ion activity coefficients, the GEM-Selektor employed the extended Debye-Huckel equation [67, 68].

$$Log_{10}\gamma_j = \frac{-A_\gamma z_j^2\sqrt{I}}{1+\dot{a}B_\gamma\sqrt{I}} + b_\gamma I + log_{10}\frac{x_{jw}}{X_w} \qquad (26)$$

where:

- γ_j – the activity coefficient
- z_j – the charge
- j – the aqueous species
- A_γ, B_γ – the electrostatic parameters
- I – the ionic strength
- x_{jw} – the mole quantity of water
- X_w – the total mole amount of the aqueous phase
- $\dot{a}$ – the average ion size

- b_γ – the parameter for common short-range interactions of the charged species

It is reported that the accuracy of the calculation results by the extended Debye-Huckel equation depends on the ionic strength (*I*). The degree of accuracy is great when *I* is from ~1 to 2 mol/L [71]. For the pore solutions in AAS, *I* is about ~1-3 mol/L [72], slightly exceeding the range of ~1-2 mol/L. Although the ion activity coefficients can be determined via the Pitzer model for solutions with high values of *I* [73], the Pitzer model is not applicable currently in GEM-Selektor. This is because the database of GEM-Selektor only considers monomeric and dimeric aqueous species [23]. In fact many researchers have employed GEM-Selektor to simulate the reactions in AAS, and a good fit was found between the simulation results and the experimental data [25, 26, 69]. So, a small increase of *I* (> 2 mol/L) is not supposed to affect the thermodynamic modelling results very much.

In GeoMicro3D the quantified reaction products, via the *thermodynamic modelling module*, were assumed to deposit *directly* into the lattice cell until it is totally full. The growth rate of reaction products in the current GeoMicro3D was not considered. Regarding this issue further research is needed in the future. In order to consider the influence of reactions of ions on the diffusion of ions, the amount of the consumed ions are deducted from the source terms in the *dissolution module*. In the meanwhile the solid phase and pore solution composition in each lattice cell are renewed.

2.5. Influence of temperature

The diffusion of ions and the rate of dissolution are seriously affected by temperature. In

GeoMicro3D the temperature effects are considered according to the Arrhenius equation.

$$D_{new} = D_{ref} exp\left[\frac{E_{diff}}{R}\left(\frac{1}{T_{ref}} - \frac{1}{T_{new}}\right)\right] \qquad (27)$$

$$r_{D,new} = r_{D,ref} exp\left[\frac{E_a}{R}\left(\frac{1}{T_{ref}} - \frac{1}{T_{new}}\right)\right] \qquad (28)$$

where:

- D_{new} – the new diffusion coefficient

- D_{ref} – the reference diffusion coefficient

- $r_{D,new}$ – the new rate of dissolution

- $r_{D,ref}$ – the reference rate of dissolution

- T_{new} – the new Kelvin temperature

- T_{ref} – the reference Kelvin temperature

- R – the gas constant

- E_{diff} – the activation energy of diffusion

- E_a – the activation energy

Besides the diffusion of ions and the rate of dissolution, temperature also affects the thermodynamic data of phases in thermodynamic modelling. In the *thermodynamic modelling module*, the thermodynamic data for phases other than 25 °C are obtained based on the data at 25 °C. Here 25 °C is the reference temperature. More information on this point can be referred to [74].

2.6. Water retention of the C-(N-)A-S-H gel

The C(N)ASH_ss model is a thermodynamic model. The H_2O content of the C(N)ASH_ss end-members refers to the water content in the solid nano-scale C-S-H. It only considers hydroxyl groups and the H_2O retained in the interlayer space of the C-(N-)A-S-H gel. In other words it does not include any adsorbed or gel pore water (see Fig. 8). In order to calculate the capillary porosity of AAS, the amounts of absorbed water and gel pore water retained by C-(N-)A-S-H must be determined additionally. In GeoMicro3D the adsorbed water and gel pore water are considered via the methods below:

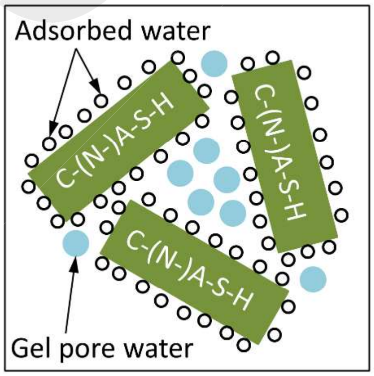

Fig. 8. Schematic representation of the adsorbed water and gel pore water retained by the C-(N-)A-S-H gel.

2.6.1 Adsorbed water

For considering the adsorbed water, 0.3 moles of water is added to each mole of C-(N-)A-S-H gels in GeoMicro3D. The density of the added water is 1.1 g/cm^3. It is noted that this method has been already employed in calculation of the chemical shrinkage of alkali-activated slag [24]. The density of the absorbed water is slightly larger than that of the bulk water (1.0 g/cm^3). This is because the absorbed water increases its effective density during the reaction of AAS.

2.6.2 Gel pore water

In the literature there is a death of information regarding the amount of gel pore water retained in C-(N-)A-S-H. To authors' knowledge so far, the amount of gel pore water retained in C-(N-)A-S-H is still unknown. On the contrary, Thomas et al. used $H_2O/SiO_2 = 4$ to consider the water that is retained in the gel pores of C-S-H during the hydration of C_3S or C_2S [75]. In the C(N)ASH_ss model, the molar H_2O/SiO_2 ratio of the C(N)ASH_ss end-members in Table 2 varies from 0.792 to 2.5, which is much smaller than 4. In order to make the GeoMicro3D model implementable, additional water is added to make the C-(N-)A-S-H gel meet the condition $H_2O/SiO_2 = 4$. The density of the added water is 1 g/cm^3. This amount of additional water represents the gel pore water retained by the C-(N-)A-S-H gel in GeoMicro3D. This method is sensible because the C-(N-)A-S-H gel is structurally similar to the C-S-H gel [20], indicating comparable amounts of gel pore water. In the future, the GeoMicro3D model can be improved in view of the amount of gel pore water retained in the C-(N-)A-S-H gel, once more information is known about the gel pore water in the C-(N-)A-S-H gel.

2.7. GeoMicro3D: the overall flowchart

Fig. 9 displays the overall flowchart of the GeoMicro3D model. It contains three parts. The first part is about the input data. The input data from slag are the chemical composition, particle size distribution, amorphous content, and density of slag. Regarding the input data from alkaline activator, the chemical composition as well as the density are required. Besides these input data, the liquid-to-slag mass ratio and reaction temperature are also needed.

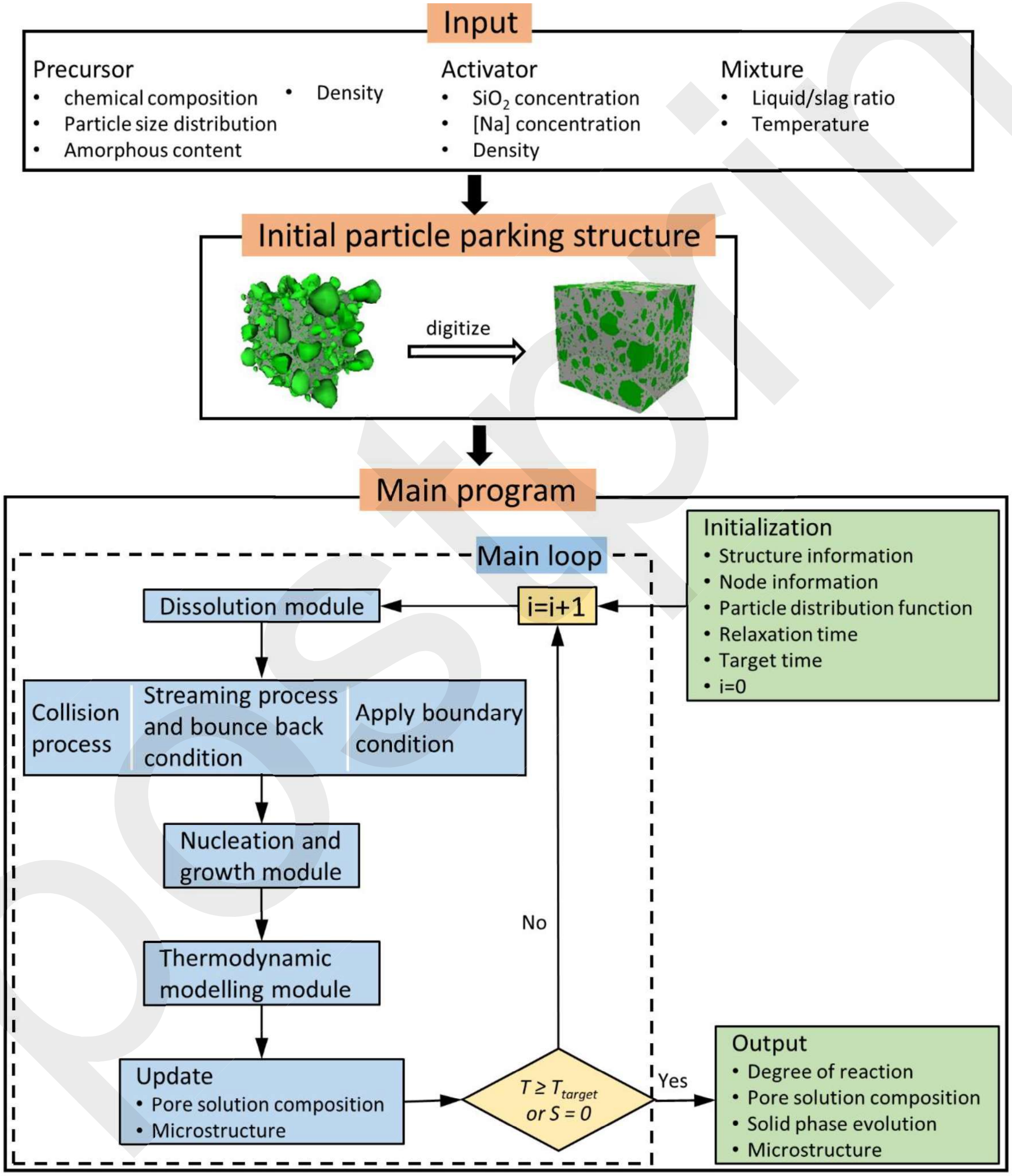

Fig. 9. The overall flowchart of the GeoMicro3D model.

The second part describes the simulation of the initial spatial distribution of real-shape slag particles in alkaline activator before the onset of reactions. First the Anm material model described in Section 2.1 is used to simulate the initial spatial distribution of slag particles in a simulation box, within which the space other than the space occupied by slag particles are regarded as alkaline activator solution. Then the simulation box is digitized into a box of voxels. Afterwards the element composition in each voxel is determined based on the mixture composition. The composition of alkaline activator is used to initialize the element constituents in the voxels that contain alkaline activator solution. In the same way, the element constituents in each slag voxel is determined based on the element composition of slag.

The main part of the GeoMicro3D model is described in the third part. The main program includes the *dissolution module*, *nucleation and growth module* and *thermodynamic modelling module*. These three modules make up the main loop in which the LB method is used to simulate the diffusion of ions. In the *dissolution module*, the dissolution of slag is simulated via the transit state theory and the diffusion of ions is described by the LB method (see Section 2.2). The LB method in simulating the diffusion of ions includes three steps: collision process, streaming process and applying boundary condition. After simulating the diffusion of ions, the element composition in each voxel are renewed. Then the voxels within which reaction products will deposit are determined via the *nucleation and growth module*. Once the voxels where reaction products will deposit are known, the *thermodynamic modelling module* is called to model the reactions and determine the amount of reaction products in these voxels. Afterwards, the solid phase and liquid phase are renewed. The consumed ions (minus) and the ones released from slag (plus) will make up the source terms for the next LB simulation iteration. Whether moving to the next iteration step or not is determined by one judgement. If the current reaction time exceeds the target reaction time or the source terms (*S*) are *zero*, then the main loop will stop and simulation results are output. *Otherwise* another iteration will start. The output data comprise but not limited to the solid phase assemblage and 3D microstructure evolution. Since the dissolution of slag and reactions of ions are fundamentally described in the unit of voxel, the interactions between different slag particles can be intrinsically dealt with.

3. Implementation and verification of the GeoMicro3D model

3.1. Materials and mixtures

Three mixtures of AAS were used in the simulation. In these mixtures sodium hydroxide solution and sodium silicate solution were the alkaline activators. The mix compositions of these mixtures are given in Table 5. In the codes for these samples, N and S mean the mass percentages of Na_2O and SiO_2 relative to slag, respectively. The chemical composition and particle size distribution of slag can be found in [54]. The density of slag was determined as 2.97 g/cm^3 by pycnometer. The surface area of slag was measured as 2.38 m^2/g by BET-nitrogen adsorption.

Table 5 Mix composition of the alkali-activated slag for simulation

Mixture	Slag (g)	Na_2O (g)	SiO_2 (g)	Water (g)
N4S0	100	4	0	40
N6S0	100	6	0	40
N6S5.4	100	6	5.4	40

3.2. Simulation parameters

With the Anm material model (see Section 2.1) and mixture composition in Table 5, the initial spatial distribution of slag particles in alkaline activator was generated and the simulation box was digitized as shown in Fig. 10. Since the maximum particle size of slag is 45 μm, the dimension size of REV in this study was selected as 125 μm. It should be noted that this selected dimension size of REV is larger than that usually used in the numerical studies of OPC based materials, for instance in HYMOSTRUC (100 μm) [12, 15]. The digitized simulation box was initialized in terms of element compositions for liquid voxels and slag voxels. Then the simulation box was used as the input for simulating the reaction process and microstructure formation of AAS with GeoMicro3D. It should be pointed out that the current GeoMicro3D model does not consider the effect of chemical shrinkage on the diffusion of ions and precipitation of reaction products. Instead additional water with density of 1 g/cm^3 is assumed to automatically fill up the empty space that is caused by chemical shrinkage.

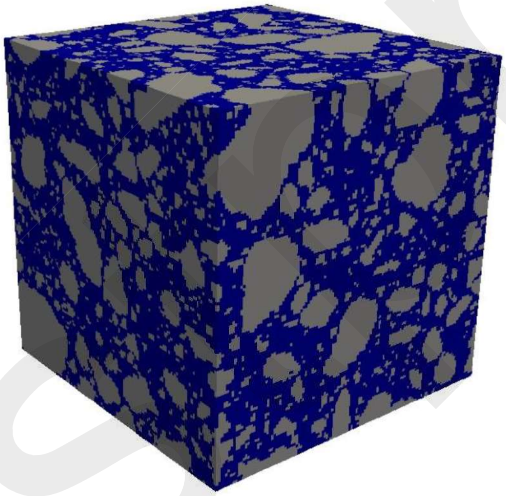

Fig. 10. Simulated initial spatial distribution of slag in alkaline activator using the Anm model in Section 2.1. In the graph, blue and gray represent activator and slag, respectively. The size of the simulation box is 125 μm × 125 μm × 125 μm. The digitization resolution is 1 μm × 1 μm × 1 μm per voxel.

In accord with [76, 77], the E_a of Si and Al for dissolution are taken as 8.3×10^4 J/mol and 8.0×10^4 J/mol, respectively. The E_a of Ca for dissolution is 1.36×10^4 J/mol [78]. The parameters f_{Mg}, f_S, f_K and f_{Na} are 1.1, 1.1, 1.2 and 1.2, respectively. In consistent with [79], $\sigma = 1$. In order to account for the effect of precipitation of reaction products on dissolution, the K_{sp} of SiO_2, Al_2O_3 and CaO are 1.89×10^{-3}, 2.47×10^{-4} and 5.31×10^{-2}, respectively. The log forward dissolution rates of silica and calcium oxide are calculated according to [80]. The parameter $f_{dissolving\text{-}area}$ is assumed to be 1.1 times of the volume fraction of solution phase in the voxel that is in contact with the dissolving interface. The diffusion coefficients and the activation energy of diffusion of ions are presented in Table 6.

Table 6 Diffusivities of aqueous ions at 25 °C [81, 82]

Ions	SiO_3^{2-}	AlO_2^-	Ca^{2+}	Mg^{2+}	S^{2-}	K^+	Na^+	OH^-
D_{ref} ($\times 10^{-9}$ m^2/s)	0.7[a]	0.6[b]	0.72	0.71	1.01[c]	1.96	1.33	5.28
E_{diff} ($\times 10^4$ J/mol)[d]	2.46	2.04	2.32	1.26	1.43	1.60	1.67	1.80

a. This value was taken from the diffusivity of $H_2SiO_4^{2-}$;

b. This value was taken from the diffusivity of Al^{3+};

c. This value was taken from the diffusivity of SO_4^{2-};

d. The activation energy of diffusion of aqueous ions were calculated based on [83-85].

Table 7 presents the kinetic parameter A. It is noted that this parameter was determined through the parameter study in the current GeoMicro3D. This is because the kinetic parameter (A) of nucleation for reaction products have not been reported in the current literature. In the future this parameter is recommended to be determined by other techniques, for example by experimental techniques [51]. The activity factor ψ is 0.27. The thermodynamic data presented in Section 2.4 for thermodynamic modelling of the chemical reactions in AAS are also used in GeoMicro3D.

Table 7 Kinetic parameter A

	C(N)ASH_ss	M_4AH_{10}	M_6AH_{12}	M_8AH_{14}	C_3AH_6	C_2ASH_8	CH	Natrolite
A (m$^{-3}\cdot$s^{-1})	4.24×10^{7}	5.01×10^{-26}	4.71×10^{-51}	2.51×10^{-71}	27.6	0.101	4.71×10^{9}	9.62×10^{3}

3.3. Simulation results

In the following sections the modelling output from GeoMicro3D are reported and examined mainly in terms of the volume evolution of phases, 3D microstructure evolution, pore structure and in particular of the output data for sample N4S0 at an age of 28 days. In the meantime, relevant experimental data and calculation results with GEMS are also presented to verify the GeoMicro3D model.

3.3.1 Volume evolution of phases

Fig. 11 presents the simulated volume proportion of phases with GeoMicro3D as a function of time, in comparison with the calculated results using GEMS. It is noted that Fe is not included in GeoMicro3D. This is because the amount of Fe in slag is very small and also for the purpose of decreasing the computation load. Furthermore the calculated results by GEMS (see Fig. 11(right column)) show that AAS did not produce much mackinawite (FeS) and brucite ($Mg(OH)_2$). Therefore, the GeoMicro3D model did not take mackinawite and brucite into account.

An overall fit can be found between the simulated phase assemblage by GeoMicro3D and the calculated results by GEMS. The C-(N-)A-S-H gel by GeoMicro3D, including the adsorbed water and gel pore water accounted for more than 60 % of the total volume of reaction products. On the contrary, the C-(N-)A-S-H gel alone accounted for more than 60 % of the total volume of reaction products as calculated using GEMS. This is because the adsorbed water and gel pore water were not considered in the thermodynamic modelling using GEMS. Other than the C-(N-)A-S-H gel, the hydrotalcite-like phase (MA-OH-LDH) accounted for the largest volume proportion. Fig. 11(left column) shows the formation of natrolite in all samples and the sample with a higher Na_2O content had a larger amount of natrolite. According to Fig. 11(right column), however, natrolite only appeared in sample N6S5.4. This difference may result from the fact that concurrent dissolution of slag was assumed in the calculations with GEMS. Fig. 11(left column) also reveals that portlandite appeared in all samples. The sample with a higher Na_2O content had a larger amount of portlandite, while the sample with an addition of SiO_2 had a lower amount of portlandite. This simulation result by GeoMicro3D agrees well with the calculated volume proportion by GEMS. In addition to the solid reaction products, the volume proportion of the adsorbed water and gel pore water were also obtained as a function of time by GeoMicro3D.

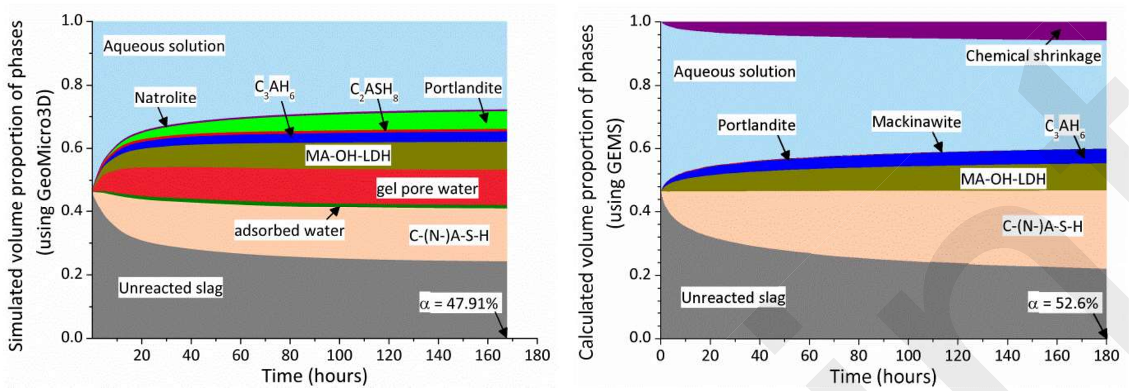

(A) N4S0, using GeoMicro3D (B) N4S0, using GEMS

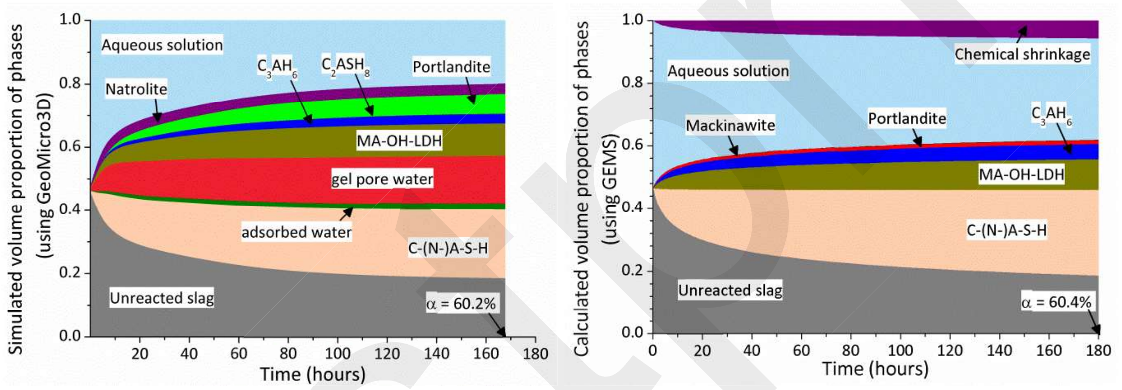

(C) N6S0, using GeoMicro3D (D) N6S0, using GEMS

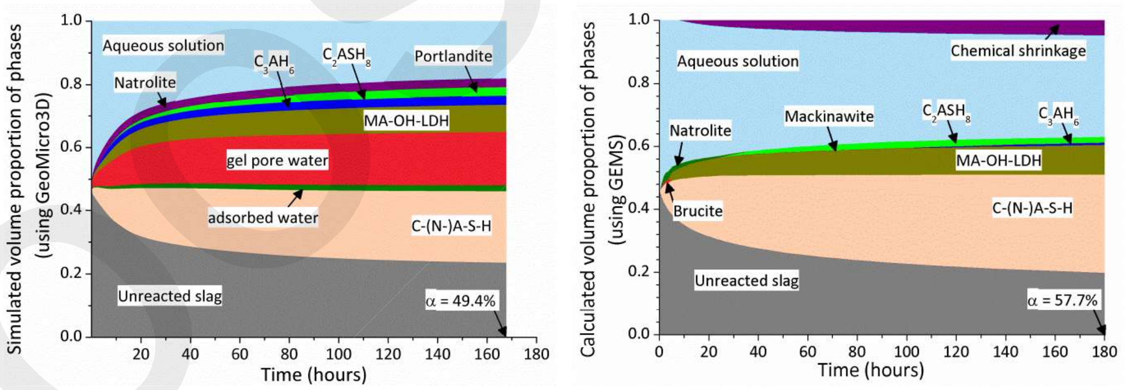

(E) N6S5.4, using GeoMicro3D (F) N6S5.4, using GEMS

Fig. 11. Simulated volume proportion of phases with GeoMicro3D in comparison with the calculation results using GEMS.

3.3.2. Microstructure development

Fig. 12 displays the simulated microstructure for sample N4S0 at four different reaction periods. The results for samples N6S0 and N6S5.4 can be found in Appendix B (see Figs. B.1 and B.2). The blue and gray voxels refer to liquid and slag, respectively. The yellow voxels are the reaction front where the dissolution of element constituents in slag may take place and in the meantime reaction products may also deposit. The red and green voxels indicate partially and completely filled with reaction products, respectively. The graphs in Fig.12 show the continuous growth of reaction products with elapse of time.

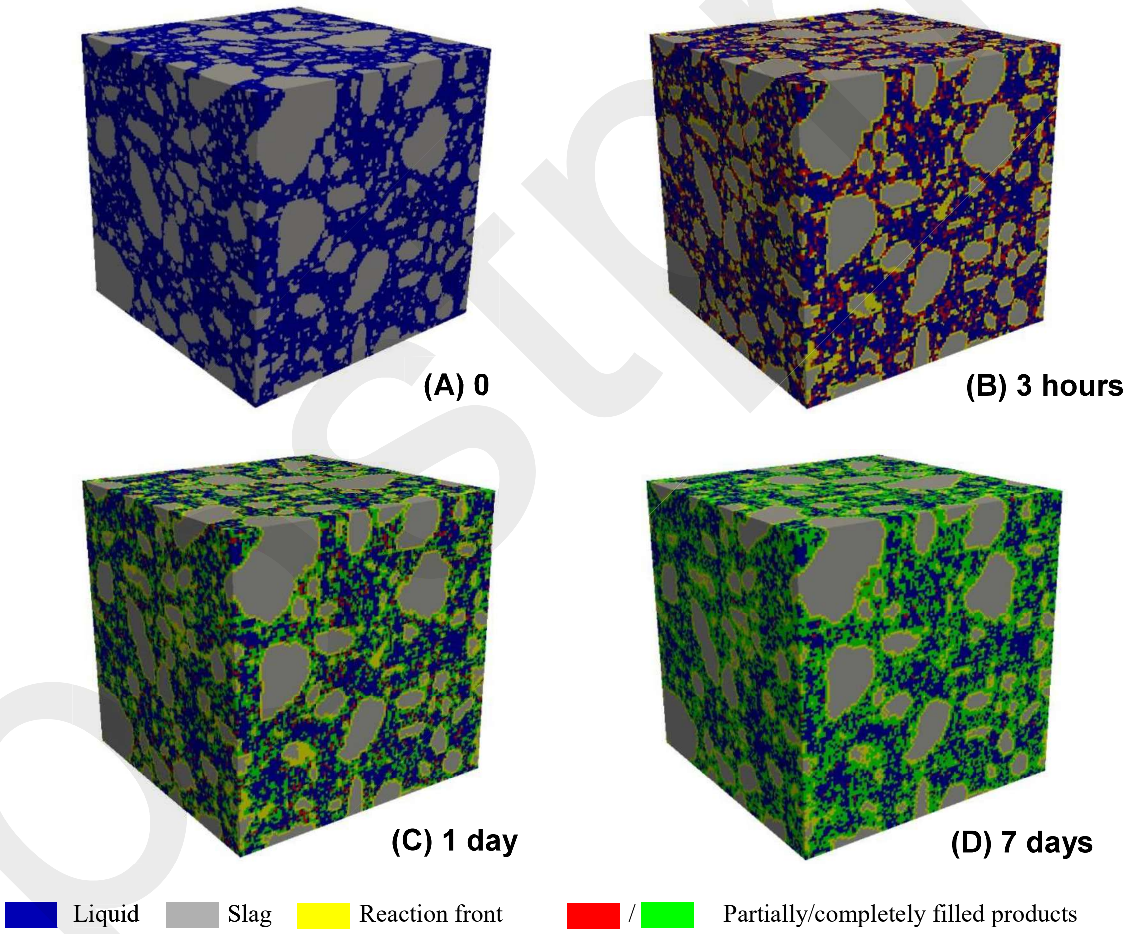

Fig. 12. Simulated 3D microstructures of sample N4S0 at 0, 3 hours, 1 day and 7 days. The simulated microstructures for samples N6S0 and N6S5.4 can be found in Appendix B (see Figs. B.1 and B.2). The size of the simulation box is 125 μm × 125 μm × 125 μm. The digitization resolution is 1 μm × 1 μm × 1 μm per voxel.

It is reported that SiO_2 in the alkaline activator obviously altered the microstructure formation of AAS [27, 52, 53]. For the purpose of convenient comparisons, the cross sections of the simulated 3D microstructures are presented for the samples N6S5.4 and N6S0 in Fig. 13. These two samples had similar degrees of reaction of slag, i.e. $\alpha = 0.335$ for N6S5.4 and $\alpha = 0.317$ for N6S0. Compared with the sample with no SiO_2 (N6S0), the reaction products were more evenly dispersed in the sample with SiO_2 (N6S5.4). This result agrees well with the SEM-image based observations in the literature [27, 52, 53].

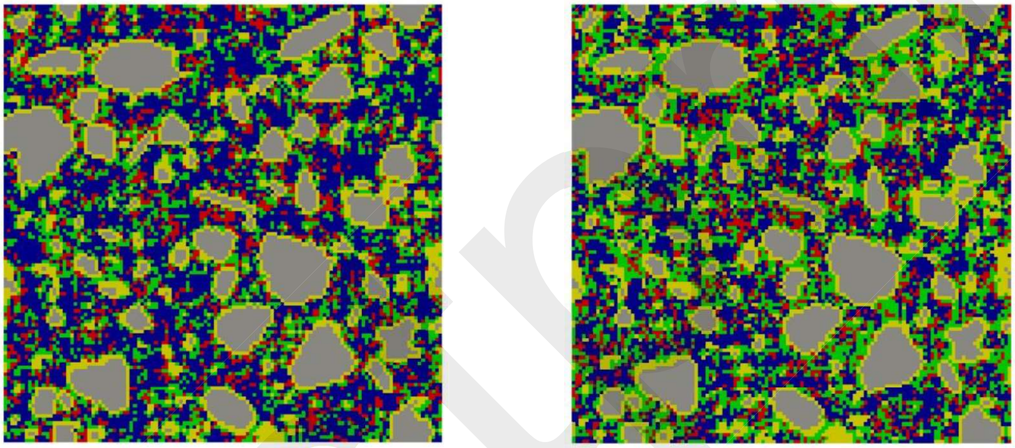

(A) N6S0, $\alpha = 0.317$ (B) N6S5.4, $\alpha = 0.335$

🟦 Liquid ▨ Slag 🟨 Reaction front 🟥 / 🟩 Partially/completely filled products

Fig. 13. Cross sections of samples N6S0 and N6S5.4 at similar degrees of reaction of slag.

Furthermore the GeoMicro3D model is also able to output the spatial distribution of reaction products in the sample. Fig. 14 displays the spatial distributions of primary reaction products for N4S0 at three different reaction periods. It is noted that the adsorbed water and gel pore water are also contained in the primary reaction products. The simulated spatial distributions of the primary reaction products for samples N6S0 and N6S5.4 can be found in Appendix B (see Figs. B.3 and B.4). It can be seen that the primary reaction products were more likely to grow on the surface of slag particles in the samples without SiO_2, i.e. N4S0 and N6S0. In contrast, the primary reaction products were evenly dispersed – not only around the slag particles but also in the interspace in the sample with SiO_2, i.e. N6S5.4. These results are in line with the observations found from the SEM-images [27, 52, 53].

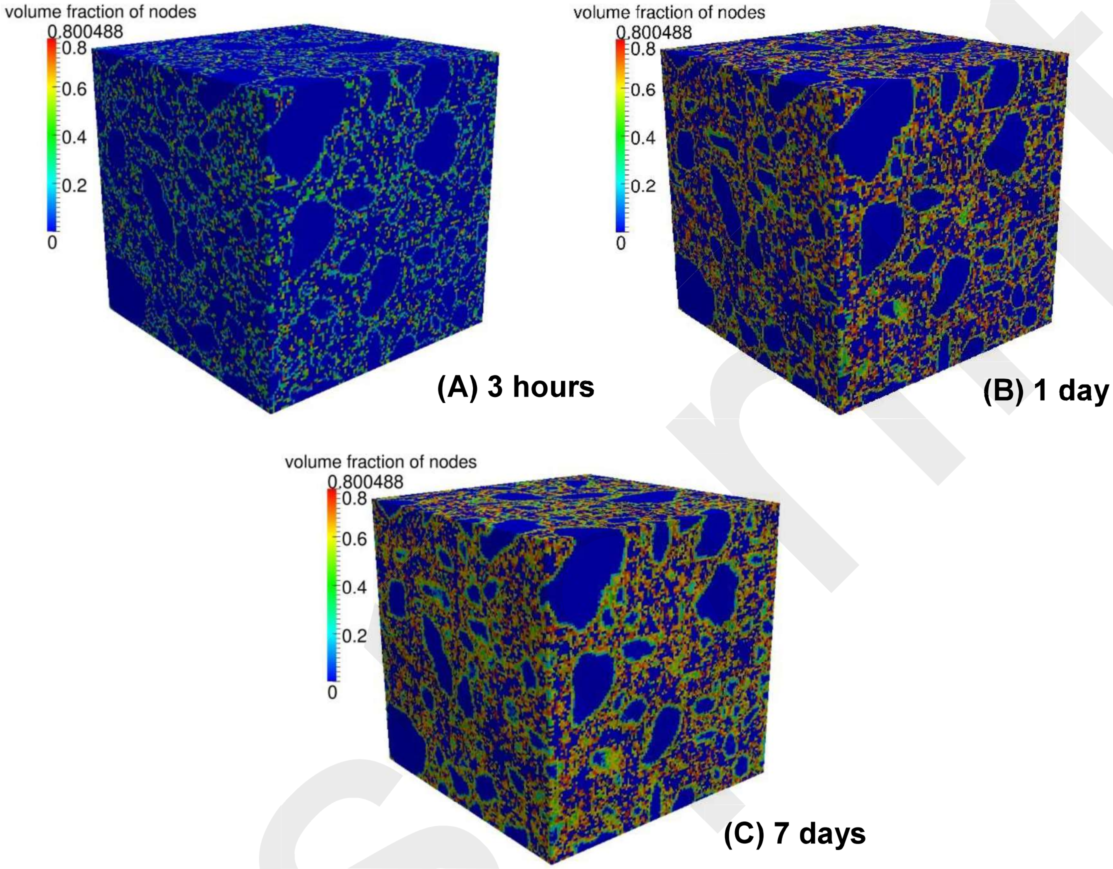

Fig. 14. Spatial distribution of the primary reaction products (including adsorbed water and gel pore water) for sample N4S0 at 3 hours, 1 day and 7 days. Volume fraction of nodes means the volume fraction of the primary reaction products in the node voxel. The results for samples N6S0 and N6S5.4 can be found in Appendix B (see Figs. C.3 and C.4). The size of the simulation box is 125 µm × 125 µm × 125 µm. The digitization resolution is 1 µm × 1 µm × 1 µm per voxel.

3.3.3. Porosity and pore size distribution

Fig. 15 displays the simulated capillary porosity. In GeoMicro3D, the volume fraction of liquid voxels was calculated as the capillary porosity. The capillary porosity decreased when the Na_2O

content in the sample increased. For the samples at the same content of Na_2O, i.e. N6S0 and N6S5.4, the sample N6S5.4 with SiO_2 had a smaller capillary porosity than the sample N6S0 without SiO_2. The reduction of porosity due to the increase of Na_2O and SiO_2 contents are in line with the observations in [52-54]. Since the porosity data determined by SEM image analysis (SEM-IA) and mercury intrusion porosimetry (MIP) in [52-54] are not exactly corresponding to the capillary porosity simulated by GeoMicro3D, it is not very sensible to directly compare the simulation results and experimental data. Therefore, these experimental data are not presented here.

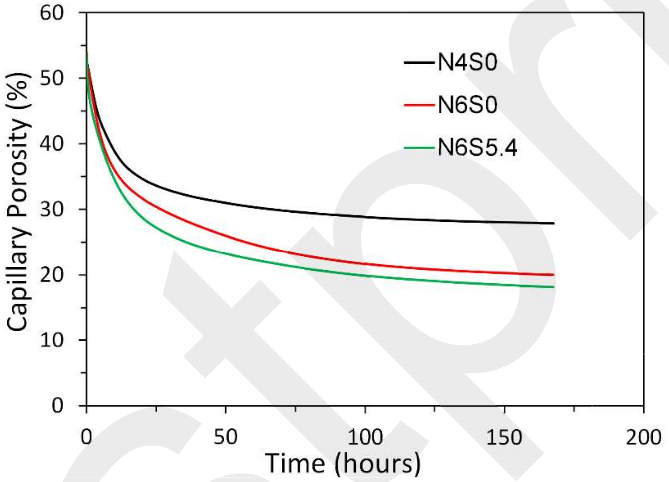

Fig. 15. Simulated capillary porosity with GeoMicro3D.

The calculated pore size distribution curve is presented in Fig. 16. It can be seen that a longer reaction time resulted in a smaller porosity and a left shift of the distribution curve. The decrease of porosity and left shift of distribution curve were also found for the samples with higher Na_2O content and SiO_2 content. The decrease of porosity and left shift of distribution curve indicate that the microstructure became denser with increasing contents of Na_2O and SiO_2 in the sample and with a longer reaction time. These simulation findings agree with the SEM observations reported in [52, 53].

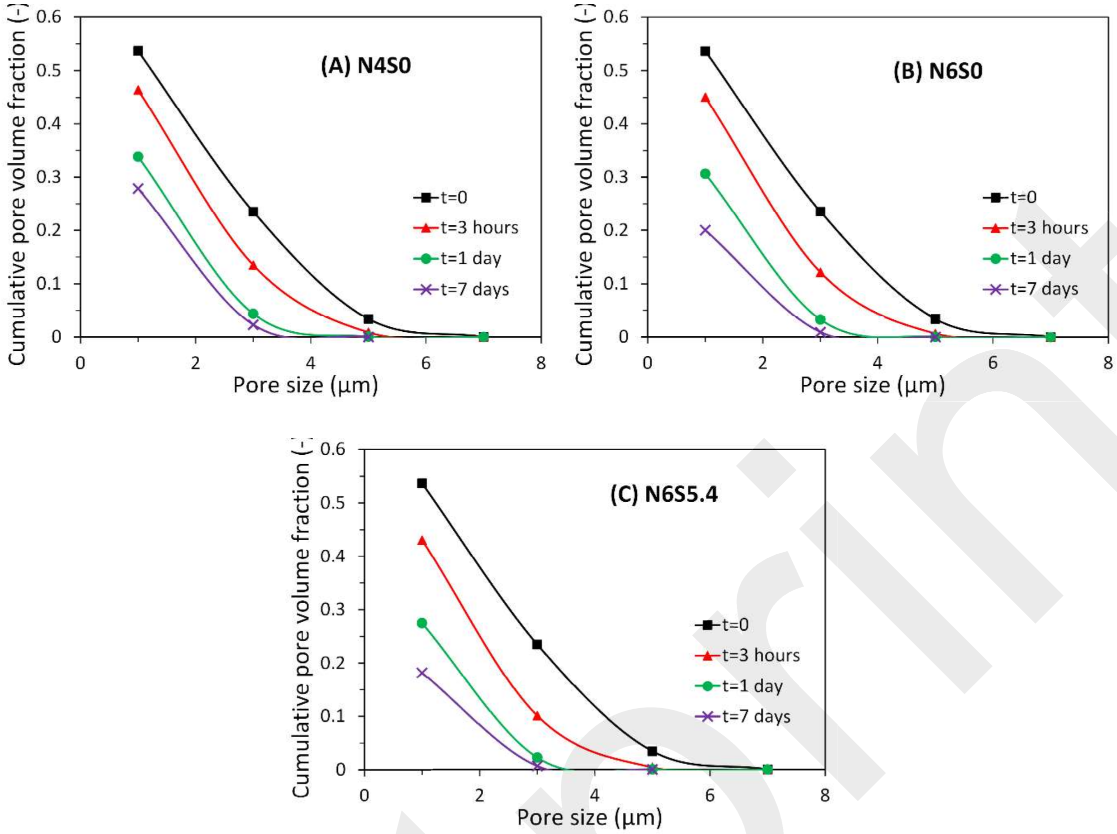

Fig. 16. Calculated pore size distribution from the simulated 3D microstructure with GeoMicro3D.

3.3.4 Simulation results of sample N4S0 at an age of 28 days

The simulation output by GeoMicro3D and the corresponding measured data are listed in Table 8 for sample N4S0 at 28 days. Overall a reasonable fit was found between the simulation output and the corresponding measured data. Compared with the measured data, the degree of reaction of slag and capillary porosity of AAS were a little underestimated and overestimated, respectively, by GeoMicro3D. This difference may be due to the assumption that water is supposed to automatically fill up the empty space that is caused by the chemical shrinkage. As a result the OH^- ions around slag particles was diluted, which decreased the alkalinity and thus retarded the dissolution of element constituents in slag. Due to the retarded dissolution of element constituents in slag, the degree of reaction of slag became smaller as opposed to the measured data. A smaller degree of reaction of slag then led to a smaller amount of reaction products. This, consequently, caused the simulated capillary porosity to be larger than the measured data. Compared with the measured element concentrations, the data output from GeoMicro3D were found to be within ± 1 order of magnitude. This discrepancy is close to the error of the measured data by experimental techniques [23].

Table 8 Simulation results of sample N4S0 at an age of 28 days in comparison with experimental results

Item		GeoMicro3D	Experiment
Degree of reaction		0.485	0.573(0.051)[a]
Capillary porosity		0.274	0.194[b]
Element concentration (mmol/L)	[Si]	11.6	3.73[c]
	[Al]	16.3	7.46
	[Ca]	6.93	0.756
	[K]	61.8	81.2
	[Na]	1.52×10^{3}	1.75×10^{3}
	[OH^-]	1.21×10^{3}	1.29×10^{3}

a. Obtained by SEM-image analysis. The number in the bracket is the deviation [54].

b. Obtained by MIP [54].

c. The measured concentrations of Si, Al, Ca, K and Na were obtained by inductively coupled plasma optical emission spectroscopy (ICP-OES), while the measured concentration of OH^- was obtained by titration against hydrochloride acid (0.1 mol/L) [86].

4. Conclusions and perspectives

For the first time the GeoMicro3D model was developed to simulate the reaction process and microstructure formation of AAS in this study. The GeoMicro3D model was built up based on four modules: (i) the simulation of the initial spatial distribution of real-shape slag particles in alkaline activator; (ii) the simulation of the dissolution of element constituents in slag and the diffusion of ions; (iii) the simulation of the spatial distribution of reaction products, in which an innovative strategy was proposed to improve the computation efficiency; and (iv) thermodynamic modelling of the chemical reactions. The GeoMicro3D model was implemented and verified by relevant experimental data and calculation results using GEMS. The solid phase assemblage output from GeoMicro3D agreed with the results obtained by GEMS. The modelling results demonstrated a decrease of porosity and a left shift of the pore size distribution curve for the sample with higher contents of Na_2O and SiO_2 and with a longer reaction time. Particularly the modelling output for sample N4S0 at an age of 28 days indicated a good fit with the experimental data in the literature [54, 86].

The developed GeoMicro3D in this study shows promising potentials for studying AAS. In future more mixtures with different sources of slag and alkaline activator composition are going to be used to further verify the GeoMicro3D model. Particularly the simulation parameters and their effects would be considered in deep details. The GeoMicro3D model may serve as a numerical simulation tool, based on which it could be feasible for researchers to numerically study and predict many microstructure-related-physical-properties of AAS.

Declaration of competing interest

The authors declare that they have no conflict of interest.

Acknowledgements

The first author would like to gratefully acknowledge the China Scholarship Council (the Grant Number 201406160086) for the financial support in this work. A special note of appreciation goes to Prof. Klaas van Breugel (Delft University of Technology, Netherlands) for his insightful comments and valuable suggestions. Many thanks go to Prof. Edward Garboczi (National Institute of Standards and Technology, USA) for providing the spherical harmonic database of slag, to Dr. Zhiwei Qian (Delft University of Technology, Netherlands) for his support and help with calculations using the Anm material model, and Mr. Jiayi Chen (Delft University of Technology, Netherlands) for the helpful discussion regarding LBM and products nucleation.

Appendix A

Transition state theory is the theory that explains the reaction rate of elementary chemical reactions. Within the framework of transition state theory, the overall dissolution rate can be written as Eq. (A.1) [87]. This equation is capable of accurately describing different dissolution behaviors of glass [38-40, 42, 79]. Since slag is a kind of aluminosilicate glass [41], transition state theory should be also applicable to describe the dissolution of slag. This point has been confirmed in the literature [44].

$$r = r_+ \left(1 - exp\left(-\frac{A^*}{\sigma RT}\right)\right) \qquad \text{(A.1)}$$

where:

- r – the overall dissolution rate

- r_+ – the forward dissolution rate

- σ – the ratio of the rate of dissolution of the activated complex relative to the overall reaction rate

- R – the gas constant

- T – the absolute temperature

- $A*$ – the chemical affinity that can be calculated as:

$$A^{*} = -RTln\left(\frac{IAP}{K_{sp}}\right) \tag{A.2}$$

where IAP and K_{sp} are the ion activity product and solubility product, respectively. With Eqs. (A.2) and (A.1) the equation below can be obtained:

$$r = r_{+}\left(1 - \left(\frac{IAP}{K_{sp}}\right)^{1/\sigma}\right) \tag{A.3}$$

Based on Eq. (A.3), the dissolution rates of silica, aluminum and calcium oxides can be obtained as expressed by Eqs. (6), (7) and (8), respectively, in Section 2.2.

Appendix B

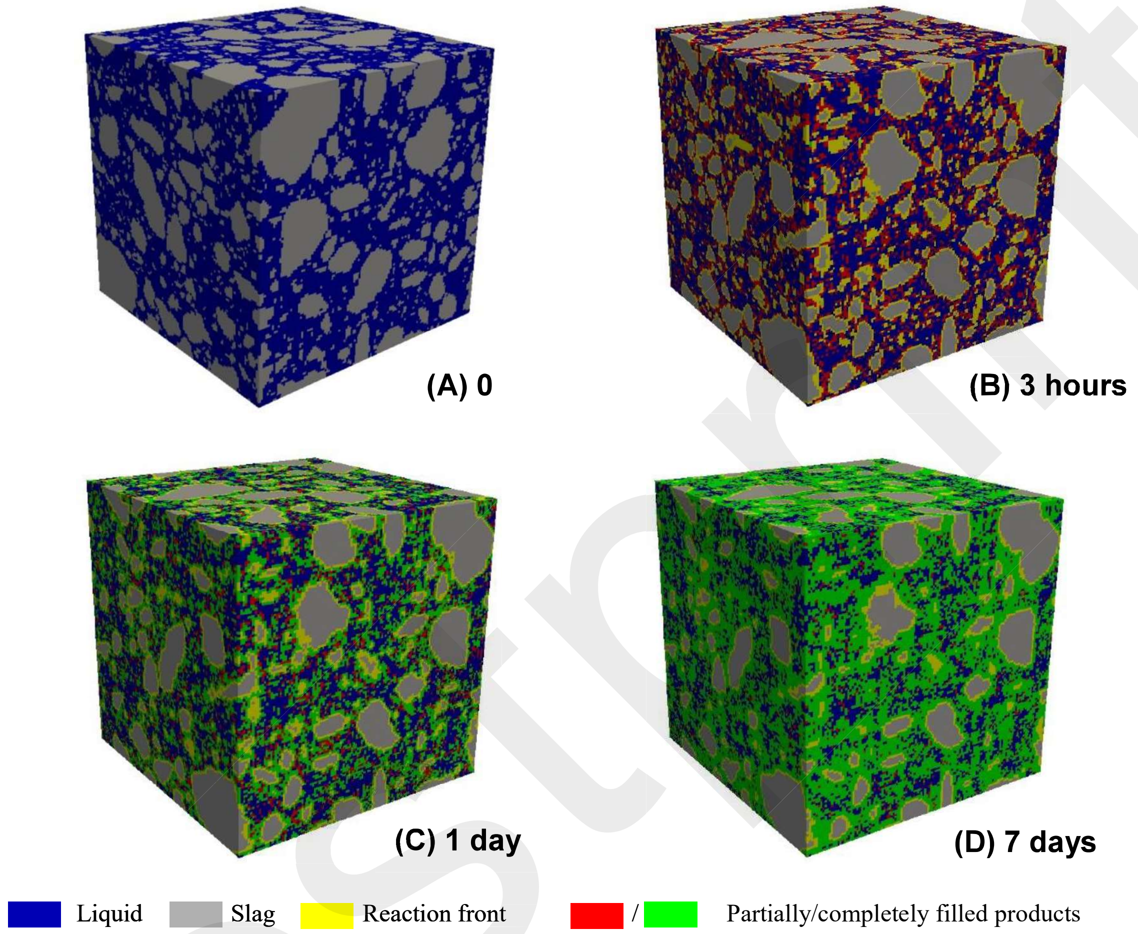

Fig. B.1. Simulated 3D microstructures of sample N6S0 at 0, 3 hours, 1 day and 7 days. The size of the simulation box is 125 μm × 125 μm × 125 μm. The digitization resolution is 1 μm × 1 μm × 1 μm per voxel.

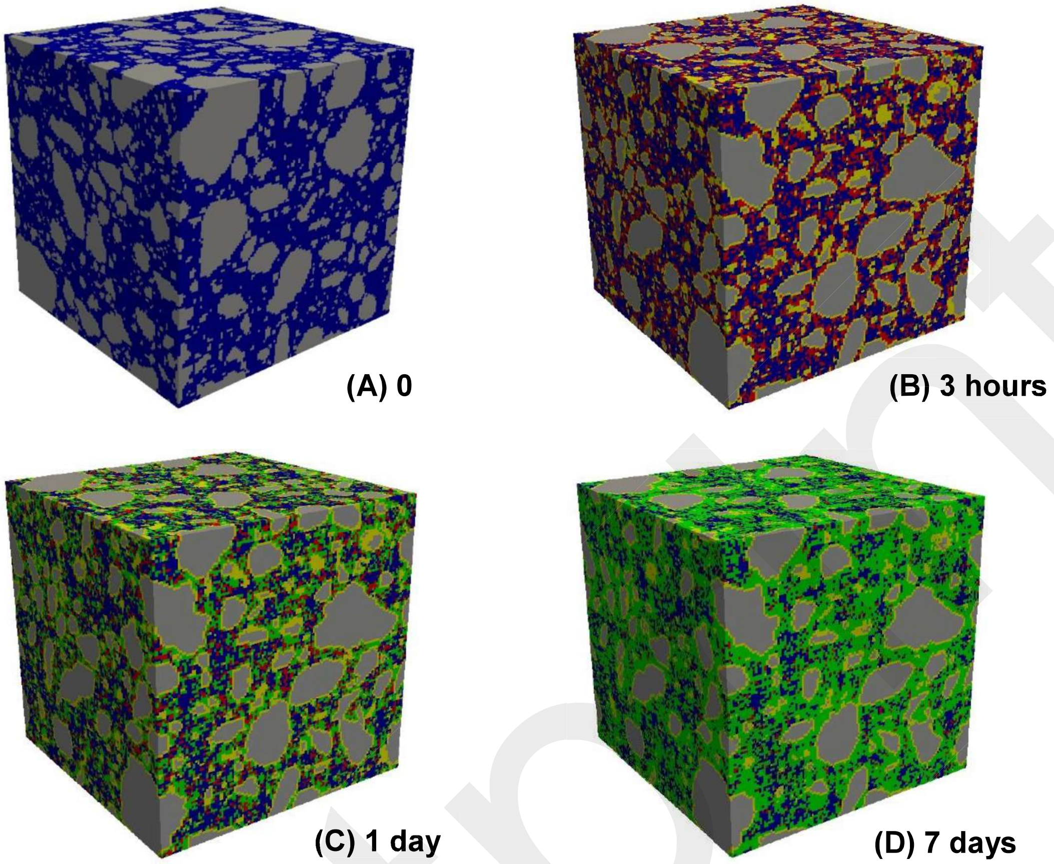

🟦 Liquid ⬜ Slag 🟨 Reaction front 🟥 / 🟩 Partially/completely filled products

Fig. B.2. Simulated 3D microstructures of sample N6S5.4 at 0, 3 hours, 1 day and 7 days. The size of the simulation box is 125 µm × 125 µm × 125 µm. The digitization resolution is 1 µm × 1 µm × 1 µm per voxel.

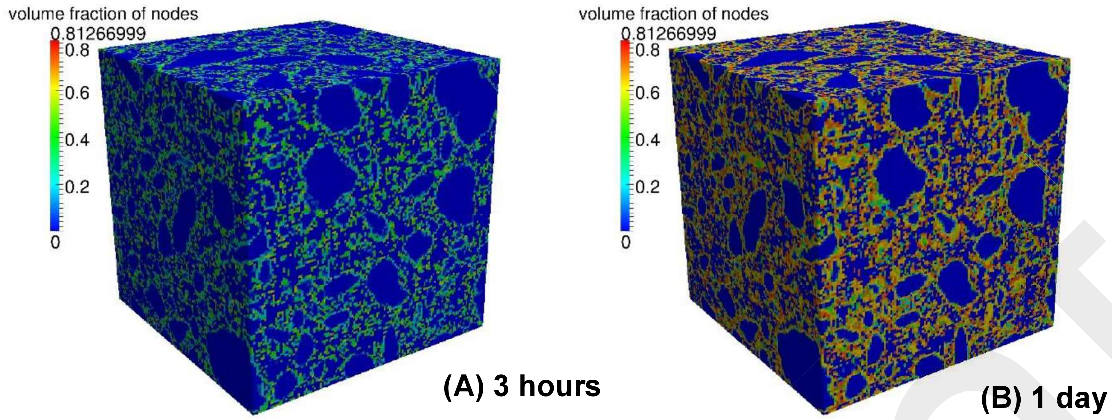

(A) 3 hours

(B) 1 day

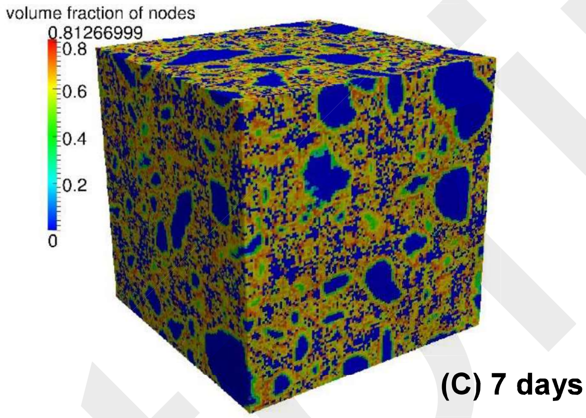

(C) 7 days

Fig. B.3. Distribution of the C-(N-)A-S-H gel (including adsorbed water and gel pore water) for sample N6S0 at 3 hours, 1 day and 7 days. Volume fraction of nodes means the volume fraction of the C-(N-)A-S-H gel in the node voxel. The size of the simulation box is 125 µm × 125 µm × 125 µm. The digitization resolution is 1 µm × 1 µm × 1 µm per voxel.

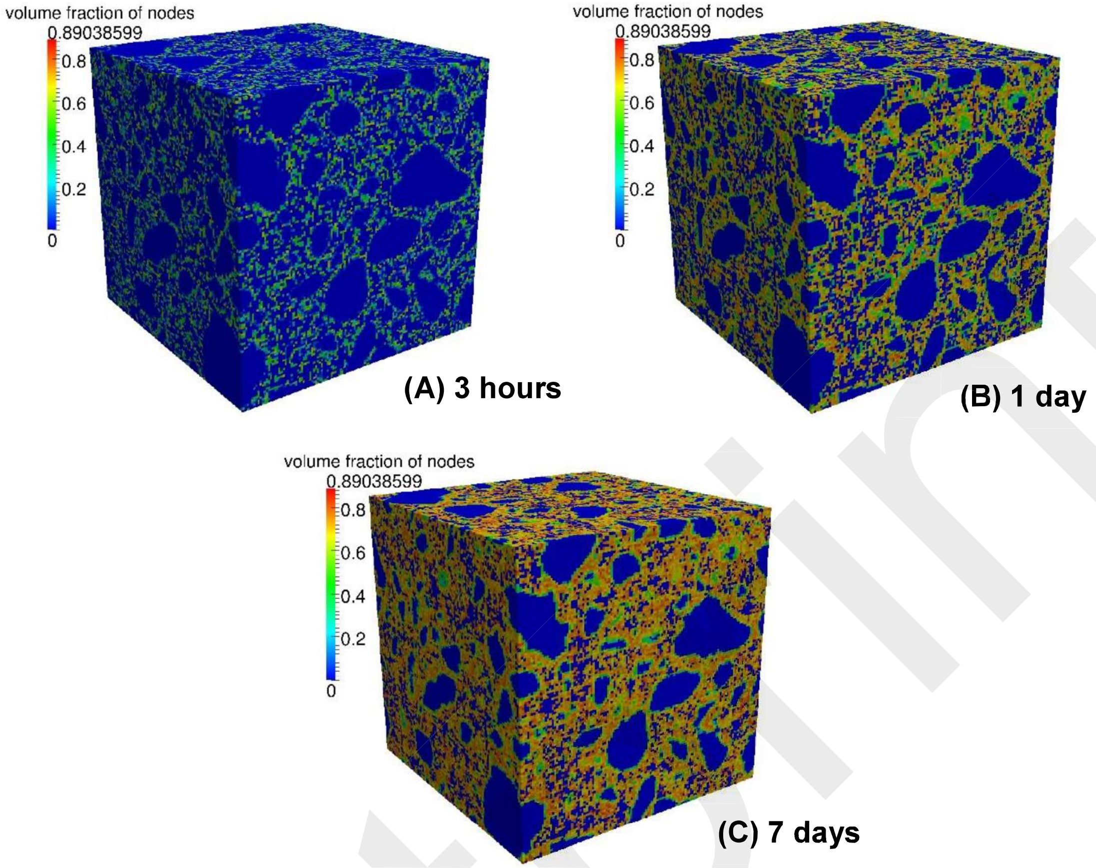

Fig. B.4. Distribution of the C-(N-)A-S-H gel (including adsorbed water and gel pore water) for sample N6S5.4 at 3 hours, 1 day and 7 days. Volume fraction of nodes means the volume fraction of the C-(N-)A-S-H gel in the node voxel. The size of the simulation box is 125 μm × 125 μm × 125 μm. The digitization resolution is 1 μm × 1 μm × 1 μm per voxel.

References

[1] S.-D. Wang, X.-C. Pu, K. Scrivener, P. Pratt, Alkali-activated slag cement and concrete: a review of properties and problems, Adv. Cem. Res. 7 (1995) 93-102.

[2] D. M. Roy, Alkali-activated cements opportunities and challenges, Cem. Concr. Res. 29 (1999) 249-254.

[3] J. S. J. van Deventer, J. L. Provis, P. Duxson, Technical and commercial progress in the adoption of geopolymer

cement, Miner Eng 29 (2012) 89-104.

[4] F. Pacheco-Torgal, J. Castro-Gomes, S. Jalali, Alkali-activated binders: A review: Part 1. Historical background, terminology, reaction mechanisms and hydration products, Constr. Build. Mater. 22 (2008) 1305-1314.

[5] L. K. Turner, F. G. Collins, Carbon dioxide equivalent (CO2-e) emissions: a comparison between geopolymer and OPC cement concrete, Constr. Build. Mater. 43 (2013) 125-130.

[6] P. Duxson, J. L. Provis, G. C. Lukey, J. S. Van Deventer, The role of inorganic polymer technology in the development of 'green concrete', Cem. Concr. Res. 37 (2007) 1590-1597.

[7] K.-H. Yang, J.-K. Song, K.-I. Song, Assessment of CO2 reduction of alkali-activated concrete, Journal of Cleaner Production 39 (2013) 265-272.

[8] F. Pacheco-Torgal, Z. Abdollahnejad, A. F. Camões, M. Jamshidi, Y. Ding, Durability of alkali-activated binders: A clear advantage over Portland cement or an unproven issue?, Constr. Build. Mater. 30 (2012) 400-405.

[9] S. A. Bernal, J. L. Provis, Durability of alkali-activated materials: progress and perspectives, J. Am. Ceram. Soc. 97 (2014) 997-1008.

[10] J. S. Dolado, K. van Breugel, Recent advances in modeling for cementitious materials, Cem. Concr. Res. 41 (2011) 711-726.

[11] J. J. Thomas, J. J. Biernacki, J. W. Bullard, S. Bishnoi, J. S. Dolado, G. W. Scherer, A. Luttge, Modeling and simulation of cement hydration kinetics and microstructure development, Cem. Concr. Res. 41 (2011) 1257-1278.

[12] G. Ye, Experimental Study and Numerical Simulation of the Development of the Microstructure and Permeability of Cementitious Materials, PhD thesis, Delft University of Technology, 2003.

[13] D. P. Bentz, Three-Dimensional Computer Simulation of Portland Cement Hydration and Microstructure

Development, J. Am. Ceram. Soc. 80 (1997) 3-21.

[14] P. Navi, C. Pignat, Simulation of cement hydration and the connectivity of the capillary pore space, Advanced Cement Based Materials 4 (1996) 58-67.

[15] K. v. Breugel, Simulation of hydration and formation of structure in hardening cement-based materials, PhD, Delft University of Technology, 1991.

[16] K. Maekawa, R. Chaube, T. Kishi, Modeling of concrete performance: hydration, microstructure formation and mass transport, E and FN SPON, London (1999)

[17] L. Liu, G. Ye, E. Schlangen, H. Chen, Z. Qian, W. Sun, K. van Breugel, Modeling of the internal damage of saturated cement paste due to ice crystallization pressure during freezing, Cem. Concr. Comp. 33 (2011) 562-571.

[18] J. L. Provis, S. A. Bernal, Geopolymers and related alkali-activated materials, Annu. Rev. Mater. Res. 44 (2014) 299-327.

[19] F. Puertas, M. Palacios, H. Manzano, J. S. Dolado, A. Rico, J. Rodríguez, A model for the C-A-S-H gel formed in alkali-activated slag cements, J. Eur. Ceram. Soc. 31 (2011) 2043-2056.

[20] R. J. Myers, S. A. Bernal, R. San Nicolas, J. L. Provis, Generalized structural description of calcium–sodium aluminosilicate hydrate gels: the cross-linked substituted tobermorite model, Langmuir 29 (2013) 5294-5306.

[21] R. J. Myers, S. A. Bernal, J. D. Gehman, J. S. Deventer, J. L. Provis, The role of Al in cross-linking of alkali-activated slag cements, J. Am. Ceram. Soc. (2015) 996-1004.

[22] P. Navi, C. Pignat, Three-dimensional characterization of the pore structure of a simulated cement paste, Cem. Concr. Res. 29 (1999) 507-514.

[23] R. J. Myers, S. A. Bernal, J. L. Provis, A thermodynamic model for C-(N-)A-S-H gel: CNASH_ss. Derivation

and validation, Cem. Concr. Res. 66 (2014) 27-47.

[24] J. J. Thomas, A. J. Allen, H. M. Jennings, Density and water content of nanoscale solid C–S–H formed in alkali-activated slag (AAS) paste and implications for chemical shrinkage, Cem. Concr. Res. 42 (2012) 377-383.

[25] R. J. Myers, B. Lothenbach, S. A. Bernal, J. L. Provis, Thermodynamic modelling of alkali-activated slag cements, Appl. Geochem. 61 (2015) 233-247.

[26] R. J. Myers, S. A. Bernal, J. L. Provis, Phase diagrams for alkali-activated slag binders, Cem. Concr. Res. 95 (2017) 30-38.

[27] H. Ye, A. Radlińska, Quantitative analysis of phase assemblage and chemical shrinkage of alkali-activated slag, J. Adv. Concr. Technol. 14 (2016) 245-260.

[28] Z. Qian, E. Garboczi, G. Ye, E. Schlangen, Anm: a geometrical model for the composite structure of mortar and concrete using real-shape particles, Mater. Struct. 49 (2016) 149-158.

[29] G. Arfken, Mathematical Methods for Physicists, 2nd, Academic Press, New York, 1970, pp.

[30] E. J. Garboczi, Three-dimensional mathematical analysis of particle shape using X-ray tomography and spherical harmonics: Application to aggregates used in concrete, Cem. Concr. Res. 32 (2002) 1621-1638.

[31] M. A. Taylor, E. J. Garboczi, S. Erdogan, D. Fowler, Some properties of irregular 3-D particles, Powder Technol. 162 (2006) 1-15.

[32] S. Erdoğan, E. J. Garboczi, D. Fowler, Shape and size of microfine aggregates: X-ray microcomputed tomography vs. laser diffraction, Powder Technol. 177 (2007) 53-63.

[33] J. M. Fernlund, The effect of particle form on sieve analysis: a test by image analysis, Engineering Geology 50 (1998) 111-124.

[34] Z. Qian, E. Schlangen, G. Ye, K. van Breugel, Modeling Framework for Fracture in Multiscale Cement-Based Material Structures, Materials 10 (2017) 587.

[35] Z. Qian, Multiscale modeling of fracture processes in cementitious materials, Delft University of Technology, 2012.

[36] Y. Zuo, Z. Qian, E. J. Garboczi, G. Ye, Numerical simulation of the initial particle parking structure of cement/geopolymer paste and the dissolution of amorphous silica using real-shape particles, Constr. Build. Mater. 185 (2018) 206-219.

[37] E. H. Oelkers, S. R. Gislason, The mechanism, rates and consequences of basaltic glass dissolution: I. An experimental study of the dissolution rates of basaltic glass as a function of aqueous Al, Si and oxalic acid concentration at 25 C and pH= 3 and 11, Geochim. Cosmochim. Acta 65 (2001) 3671-3681.

[38] E. H. Oelkers, General kinetic description of multioxide silicate mineral and glass dissolution, Geochim. Cosmochim. Acta 65 (2001) 3703-3719.

[39] S. R. Gislason, E. H. Oelkers, Mechanism, rates, and consequences of basaltic glass dissolution: II. An experimental study of the dissolution rates of basaltic glass as a function of pH and temperature, Geochim. Cosmochim. Acta 67 (2003) 3817-3832.

[40] E. H. Oelkers, J. Schott, J.-L. Devidal, The effect of aluminum, pH, and chemical affinity on the rates of aluminosilicate dissolution reactions, Geochim. Cosmochim. Acta 58 (1994) 2011-2024.

[41] P. Duxson, J. L. Provis, Designing precursors for geopolymer cements, J. Am. Ceram. Soc. 91 (2008) 3864-3869.

[42] G. Berger, C. Claparols, C. Guy, V. Daux, Dissolution rate of a basalt glass in silica-rich solutions: implications for long-term alteration, Geochim. Cosmochim. Acta 58 (1994) 4875-4886.

[43] C. Guy, J. Schott, Multisite surface reaction versus transport control during the hydrolysis of a complex oxide, Chem. Geol. 78 (1989) 181-204.

[44] R. Snellings, Solution-controlled dissolution of supplementary cementitious material glasses at pH 13: The Effect of Solution Composition on Glass Dissolution Rates, J. Am. Ceram. Soc. 96 (2013) 2467-2475.

[45] D. Wolff-Boenisch, S. R. Gislason, E. H. Oelkers, C. V. Putnis, The dissolution rates of natural glasses as a function of their composition at pH 4 and 10.6, and temperatures from 25 to 74 degrees C, Geochim. Cosmochim. Acta 68 (2004) 4843-4858.

[46] M. Zhang, Multiscale lattice Boltzmann-finite element modelling of transport properties in cement-based materials, Delft University of Technology, 2013.

[47] A. A. Mohamad, Lattice Boltzmann method: fundamentals and engineering applications with computer codes, Springer Science & Business Media,, 2011, pp.

[48] M. Zhang, G. Ye, K. van Breugel, Modeling of ionic diffusivity in non-saturated cement-based materials using lattice Boltzmann method, Cem. Concr. Res. 42 (2012) 1524-1533.

[49] N. Jeong, D. H. Choi, C.-L. Lin, Estimation of thermal and mass diffusivity in a porous medium of complex structure using a lattice Boltzmann method, Int. J. Heat Mass Transfer 51 (2008) 3913-3923.

[50] D. Kashchiev, G. Van Rosmalen, Nucleation in solutions revisited, Cryst. Res. Technol. 38 (2003) 555-574.

[51] S. Jiang, J. H. ter Horst, Crystal nucleation rates from probability distributions of induction times, Cryst. Growth Des. 11 (2010) 256-261.

[52] M. Ben Haha, G. Le Saout, F. Winnefeld, B. Lothenbach, Influence of activator type on hydration kinetics, hydrate assemblage and microstructural development of alkali activated blast-furnace slags, Cem. Concr. Res. 41

(2011) 301-310.

[53] M. B. Haha, B. Lothenbach, G. Le Saout, F. Winnefeld, Influence of slag chemistry on the hydration of alkali-activated blast-furnace slag — Part I: Effect of MgO, Cem. Concr. Res. 41 (2011) 955-963.

[54] Y. Zuo, G. Ye, Pore Structure Characterization of Sodium Hydroxide Activated Slag Using Mercury Intrusion Porosimetry, Nitrogen Adsorption, and Image Analysis, Materials 11 (2018) 1035.

[55] S.-D. Wang, K. L. Scrivener, Hydration products of alkali activated slag cement, Cem. Concr. Res. 25 (1995) 561-571.

[56] I. G. Richardson, A. R. Brough, G. W. Groves, C. M. Dobson, The characterization of hardened alkali-activated blast-furnace slag pastes and the nature of the calcium silicate hydrate (C-S-H) phase, Cem. Concr. Res. 24 (1994) 813-829.

[57] Y. Zuo, M. Nedeljković, G. Ye, Coupled thermodynamic modelling and experimental study of sodium hydroxide activated slag, Constr. Build. Mater. 188 (2018) 262-279.

[58] M. Wolthers, L. Charlet, P. R. van Der Linde, D. Rickard, C. H. van Der Weijden, Surface chemistry of disordered mackinawite (FeS), Geochim. Cosmochim. Acta 69 (2005) 3469-3481.

[59] B. Lothenbach, A. Gruskovnjak, Hydration of alkali-activated slag: thermodynamic modelling, Adv. Cem. Res. 19 (2007) 81-92.

[60] D. Bennett, D. Read, M. Atkins, F. Glasser, A thermodynamic model for blended cements. II: Cement hydrate phases; thermodynamic values and modelling studies, J. Nucl. Mater. 190 (1992) 315-325.

[61] B. Lothenbach, F. Winnefeld, Thermodynamic modelling of the hydration of Portland cement, Cem. Concr. Res. 36 (2006) 209-226.

[62] W. Gao, Z. Li, Solubility and KSP of Mg4Al2 (OH) 14· 3H2O at the various ionic strengths, Hydrometallurgy 117 (2012) 36-46.

[63] A. Anderko, P. J. Shuler, A computational approach to predicting the formation of iron sulfide species using stability diagrams, Comput. Geosci. 23 (1997) 647-658.

[64] B. Lothenbach, L. Pelletier-Chaignat, F. Winnefeld, Stability in the system CaO–Al2O3–H2O, Cem. Concr. Res. 42 (2012) 1621-1634.

[65] B. Lothenbach, E. Bernard, U. Mäder, Zeolite formation in the presence of cement hydrates and albite, Physics and Chemistry of the Earth, Parts A/B/C 99 (2017) 77-94.

[66] T. Matschei, B. Lothenbach, F. P. Glasser, Thermodynamic properties of Portland cement hydrates in the system CaO–Al2O3–SiO2–CaSO4–CaCO3–H2O, Cem. Concr. Res. 37 (2007) 1379-1410.

[67] D. A. Kulik, T. Wagner, S. V. Dmytrieva, G. Kosakowski, F. F. Hingerl, K. V. Chudnenko, U. R. Berner, GEM-Selektor geochemical modeling package: revised algorithm and GEMS3K numerical kernel for coupled simulation codes, Comput. Geosci. 17 (2013) 1-24.

[68] T. Wagner, D. A. Kulik, F. F. Hingerl, S. V. Dmytrieva, GEM-Selektor geochemical modeling package: TSolMod library and data interface for multicomponent phase models, Can. Mineral. 50 (2012) 1173-1195.

[69] R. J. Myers, Thermodynamic Modelling of CaO-Al2O3-SiO2-H2O-Based Cements, University of Sheffield, 2015.

[70] B. Lothenbach, T. Matschei, G. Möschner, F. P. Glasser, Thermodynamic modelling of the effect of temperature on the hydration and porosity of Portland cement, Cem. Concr. Res. 38 (2008) 1-18.

[71] H. C. Helgeson, D. H. Kirkham, G. C. Flowers, Theoretical prediction of the thermodynamic behavior of aqueous electrolytes by high pressures and temperatures; IV, Calculation of activity coefficients, osmotic

coefficients, and apparent molal and standard and relative partial molal properties to 600 degrees C and 5kb, Am. J. Sci. 281 (1981) 1249-1516.

[72] A. Gruskovnjak, B. Lothenbach, L. Holzer, R. Figi, F. Winnefeld, Hydration of alkali-activated slag: comparison with ordinary Portland cement, Adv. Cem. Res. (2006) 119-128.

[73] K. S. Pitzer, Ion interaction approach: theory and data correlation, Activity coefficients in electrolyte solutions, CRC Press, Roca Raton, 1991, pp. 75-153.

[74] D. A. Kulik, Minimising uncertainty induced by temperature extrapolations of thermodynamic data: a pragmatic view on the integration of thermodynamic databases into geochemical computer codes, in: F. Monpean, Proceedings of The use of thermodynamic databases in performance assessment, Barcelona, Spain, 2002, pp. 125-137.

[75] J. J. Thomas, H. M. Jennings, A. J. Allen, Relationships between composition and density of tobermorite, jennite, and nanoscale CaO− SiO2− H2O, J. Phys. Chem. C 114 (2010) 7594-7601.

[76] Y. Niibori, M. Kunita, O. Tochiyama, T. Chida, Dissolution rates of amorphous silica in highly alkaline solution, J. Nucl. Sci. Technol. 37 (2000) 349-357.

[77] A. Packter, H. Dhillon, Studies on recrystallised aluminium hydroxide precipitates, Colloid. Polym. Sci. 252 (1974) 249-256.

[78] T. Stamatis, M. Aggeliki, Hydration of CaO present in fly ashes, National Technical University of Athens, 2015 1-74.

[79] V. Daux, C. Guy, T. Advocat, J.-L. Crovisier, P. Stille, Kinetic aspects of basaltic glass dissolution at 90°C: role of aqueous silicon and aluminium, Chem. Geol. 142 (1997) 109-126.

[80] Y. Zuo, G. Ye, Lattice Boltzmann simulation of the dissolution of slag in alkaline solution using real-shape

particles, Cement and Concrete Research, 140 (2021) 106313.

[81] H. Huang, Thermodynamics of autogenous self-healing in cementitious materials, PhD, Delft University of Technology, 2014.

[82] E. L. Cussler, Diffusion: mass transfer in fluid systems, Cambridge university press, , 2009, pp.

[83] C. J. Fell, H. P. Hutchison, Diffusion coefficients for sodium and potassium chlorides in water at elevated temperatures, Journal of Chemical & Engineering Data 16 (1971) 427-429.

[84] S. A. Socolofsky, G. H. Jirka, Environmental Fluid Mechanics Part I: Mass Transfer and Diffusion, Class notes, Karlsruhe Institute of Technology,, 2002, pp.

[85] E. Goli, T. Hiemstra, W. H. Van Riemsdijk, R. Rahnemaie, M. J. Malakouti, Diffusion of neutral and ionic species in charged membranes: boric acid, arsenite, and water, Anal. Chem. 82 (2010) 8438-8445.

[86] Y. Zuo, M. Nedeljković, G. Ye, Pore solution composition of alkali-activated slag/fly ash pastes, Cem. Concr. Res. 115 (2019) 230-250.

[87] P. Aagaard, H. C. Helgeson, Thermodynamic and kinetic constraints on reaction rates among minerals and aqueous solutions: I, Theoretical considerations, Am. J. Sci. 282 (1982) 237-285.